ISSN 1991-1696

SAIEE

Africa Research Journal

Research Journal of the South African Institute of Electrical Engineers

Incorporating the SAIEE Transactions

March 2015
Volume 106 No. 1

www.saiee.org.za

SAIEE AFRICA RESEARCH JOURNAL

(SAIEE FOUNDED JUNE 1909 INCORPORATED DECEMBER 1909)
AN OFFICIAL JOURNAL OF THE INSTITUTE
ISSN 1991-1696

Secretary and Head Office
Mrs Gerda Geyer
South African Institute for Electrical Engineers (SAIEE)
PO Box 751253, Gardenview, 2047, South Africa
Tel: (27-11) 487-3003
Fax: (27-11) 487-3002
E-mail: researchjournal@saiee.org.za

Published by
South African Institute of Electrical Engineers (Pty) Ltd, PO Box 751253, Gardenview, 2047
Tel. (27-11) 487-3003, Fax. (27-11) 487-3002,
E-mail: researchjournal@saiee.org.za

Additional reviewers are approached as necessary

ARTICLES SUBMITTED TO THE SAIEE AFRICA RESEARCH JOURNAL ARE FULLY PEER REVIEWED PRIOR TO ACCEPTANCE FOR PUBLICATION

The following organisations have listed SAIEE Africa Research Journal for abstraction purposes:

INSPEC (The Institution of Electrical Engineers, London); 'The Engineering Index' (Engineering Information Inc.)

VOL 106 No 1
March 2015

SAIEE Africa Research Journal

MULTIPLE-ACCESS INTERFERENCE OF GOLD CODES IN A DS-CDMA SYSTEM

Olanrewaju B. Wojuola and Stanley H. Mneney

Centre for Radio Access and Rural Technologies (CRART), School of Engineering, University of KwaZulu-Natal, Durban 4041, South Africa.
Email: 210556350@stu.ukzn.ac.za, mneneys@ukzn.ac.za

Abstract: Properties of spreading codes constitute a limiting factor on the performance of DS-CDMA systems. In this paper, we investigate the performance of certain sets of Gold codes in a multi-user DS-CDMA system, from a few users to full system load. Simulation results show that as the system load increases, BER graphs of all the codes maintain their steep high-SNR slopes, with no emergence of error floor or significant system saturation. The results indicate that certain sets of Gold codes have good cross-correlation properties that make them resistant to multiple-access interference, making them more suitable for multiple-access applications.

Keywords: Direct-sequence code division multiple access (DS-CDMA), multiple-access interference (MAI), Gold codes, pseudo-noise encoding, bit-error-rate (BER), error floor.

1. INTRODUCTION

Code Division Multiple Access (CDMA) is a multiple-access technique that relies on coding to achieve its multiple-access property. The performance of a Direct-Sequence (DS) CDMA system depends greatly on the properties of the code sequences used for the system. The type and properties of the codes set bounds on the capability of the system. Imperfect properties of codes are known to be a cause of multiple-access interference (MAI), which happens to be an important factor limiting the capacity of DS-CDMA systems. The significance of spreading codes is applicable not only to the basic DS-CDMA system, but also other emerging modern technologies like the wideband-CDMA (WCDMA) system, the multicarrier CDMA system and its space-time-coded counterparts [1-3].

The significance of spreading codes has made the search for better spreading codes an important research subject. For example in [4-9], Hsiao-Hwa et al. proposed the design of complementary codes for CDMA systems, and later proposed an interference-cancellation method for the same [10]. Another example is in [11], where Pal and Chattopadhyay proposed an algorithm for generating orthogonal minimum cross-correlation spreading codes.

Although there exists a vast amount of published work on spread spectrum systems, as well as works relating to the design, properties, performance and generation of spreading codes [1, 8, 11-27], we are yet to see any paper that examines multiple-access performance of Gold codes as a class. We seek to fill this gap. In this paper, we investigate the performance of a set of Gold codes in a DS-CDMA system. Effects of the codes' MAI on the system bit-error-rate (BER) in a multi-user environment, ranging from a few users to tens of users, are considered. The outcome of the work gives new insight on multiple-access performance of Gold codes.

Any particular code is normally expected to have a maximum number of users that would be tolerated, a number that is believed to be well below full load. In contrast, simulation results to be presented in this paper show that with good choice of codes, the number of available codes can go up to full-load. This is an important contribution of this paper. The outcome indicates the need for careful choice of spreading codes when designing a CDMA system.

In the rest of this paper, fundamental theory is contained in Section 2, followed by research methodology in Section 3, simulation results in Section 4, discussion in Section 5, suggested future work in Section 6, and lastly, conclusion in Section 7.

2. SYSTEM MODEL

In digital DS-CDMA, the message signal is multiplied directly by the code signal and the resulting signal modulates a carrier for transmission through a communication channel. At the other end, the receiver correlates the received signal with the code of the user. Correlating the received signal with the code for a certain user de-spreads (decodes) the signal for the user.

For a DS-CDMA system, the spread spectrum signal transmitted by a user k can be expressed as

$$s_k(t) = Ac_k(t)b_k(t)\cos(\omega_c t + \theta_k), \quad (1)$$

where $b_k(t)$ is the user binary data, $c_k(t)$ is spreading code and ω_c is carrier frequency. The spreading code $c_k(t)$ for the user can be denoted as

$$c_k(t) = \sum_{i=1}^{N} c_k^i P_c(t - iT_c), \qquad c_k^i \in \{-1,1\}, \quad (2)$$

where N is length of the code, and P_c is a rectangular pulse having a duration T_c. Let the wireless communication channel be represented by multiple paths having a real positive gain β_l, propagation delay τ_l and phase shift γ_l,

where l is path index. The channel impulse response $h_k(t)$ for L independent paths can be modelled as

$$h_k(t) = \sum_{l=1}^{L} \beta_{kl} e^{j\gamma_{kl}} \delta(t - \tau_{kl}) \quad . \tag{3}$$

At the receiving end, the received signal $r_k(t)$ for the user is obtained by convolving $s_k(t)$ with $h_k(t)$ and adding noise so that

$$r_k(t) = \int_{-\infty}^{\infty} s_k(\tau) h_k(t-\tau) d\tau \; + \; n(t), \tag{4}$$

where $n(t)$ represents the channel noise. Substituting the expressions for $s_k(t)$ and $h_k(t)$ into this integral, and using relevant properties of the Dirac delta function $\delta(t)$ gives

$$r_k(t) = \sum_{l=1}^{L} A\beta_{kl} e^{j\gamma_{kl}} c_k(t-\tau_{kl}) b_k(t-\tau_{kl}). \; cos(\omega_c t - \theta_{kl}) + \; n(t) \tag{5}$$

For a multi-user system comprising K users, the received signal $r(t)$ is a linear superposition of the signals for the users, and is given by

$$r(t) = \sum_{k=1}^{K} \sum_{l=1}^{L} A\beta_{kl} e^{j\gamma_{kl}} c_k(t-\tau_{kl}) b_k(t-\tau_{kl}). \; cos(\omega_c t - \theta_{kl}) + \; n(t) \tag{6}$$

Let user-1 be the reference user. Assuming coherent demodulation, the receiver output $z(m)$ for m^{th} bit during the bit duration T_b of the user is given by

$$z_1(m) \; = \int_{mT_b}^{(m+1)T_b} r(t) c_1(t) \cos \omega_c t \, dt$$

$$= \int_{mT_b}^{(m+1)T_b} \left\{ \sum_{k=1}^{K} \sum_{l=1}^{L} A\beta_{kl} e^{j\gamma_{kl}} c_k(t-\tau_{kl}) b_k(t-\tau_{kl}). \; cos(\omega_c t - \theta_{kl}) + \; n(t) \right\} c_1(t) \cos\omega_c t \, dt$$

$$= \int_{mT_b}^{(m+1)T_b} \left\{ \sum_{l=1}^{L} A\beta_{1l} e^{j\gamma_{1l}} c_1(t-\tau_{1l}) b_1(t-\tau_{1l}) \; cos(\omega_c t - \theta_{1l}) \right\} c_1(t) \cos \omega_c t \, dt$$

$$+ \int_{mT_b}^{(m+1)T_b} \left\{ \sum_{k=2}^{K} \sum_{l=1}^{L} A\beta_{kl} e^{j\gamma_{kl}} c_k(t-\tau_{kl}) b_k(t-\tau_{kl}). \; cos(\omega_c t - \theta_{kl}) \right\} c_1(t) \cos \omega_c t \, dt$$

$$+ \int_{mT_b}^{(m+1)T_b} n(t) c_1(t) \cos \omega_c t \, dt$$

$$= \; z_{11} + z_{12} + z_{13} \tag{7}$$

where

$$z_{11} = \int_{mT_b}^{(m+1)T_b} \left\{ \sum_{l=1}^{L} A\beta_{1l} e^{j\gamma_{1l}} c_1(t-\tau_{1l}). \; b_1(t-\tau_{1l}) cos(\omega_c t - \theta_{1l}) \right\} c_1(t) \cos \omega_c t \, dt$$

$$z_{12} = \int_{mT_b}^{(m+1)T_b} \left\{ \sum_{k=2}^{K} \sum_{l=1}^{L} A\beta_{kl} e^{j\gamma_{kl}} c_k(t-\tau_{kl}). \; b_k(t-\tau_{kl}) \; cos(\omega_c t - \theta_{kl}) \right\} c_1(t) \cos \omega_c t \, dt$$

and

$$z_{13} = \int_{mT_b}^{(m+1)T_b} n(t) c_1(t) \cos \omega_c t \, dt, \tag{8}$$

where z_{11} represents the desired signal for the reference user, z_{12} is interference term, and z_{13} is noise term.

Gold codes are a type of pseudo-noise (PN) sequences derived from combination of certain pairs of m-sequences called *preferred sequences*, implemented using Linear Feedback Shift Registers (LFSR). A Gold code has a period $N = 2^n - 1$, where n is the length of the shift register. Gold codes exhibit three-valued cross-correlation function [28-30] with values {-1, -t(n), t(n)-2}, where

$$t(n) = \begin{cases} 2^{(n+1)/2} + 1, & n \text{ odd} \\ 2^{(n+2)/2} + 1, & n \text{ even.} \end{cases} \tag{9}$$

At zero shift, the autocorrelation function of the codes has the value N, where $N = 2^n - 1$; at all other phase lags, the autocorrelation takes on one of the values predicted by its cross-correlation function.

3. METHODOLOGY

Software simulations were carried out for the transmission of 64,000 random quadrature phase shift keying QPSK symbols in an additive white Gaussian noise (AWGN) channel having a zero-mean and unit variance, using Gold code-encoding for code length N = 31, 127, 511 and 2047 chips. The Gold codes were generated from appropriate combinations of preferred pairs of m-sequences (Table 1), obtained from software implementation of LFSRs. The LFSRs were pre-filled with ones. The codes used were selected in the order of generation. For example, for a simulation involving five users, the first five codes of the set concerned were used as spreading sequences for the users, with the first member of the set being for the reference user.

Table 1. Generator polynomials for the Gold codes

n	$P_i^n(x)$	*Generator polynomial	N
5	$P_1^5(x)$	$x^5 + x^2 + 1$	31
	$P_2^5(x)$	$x^5 + x^4 + x^3 + x^2 + 1$	
6	$P_1^6(x)$	$x^6 + x^5 + 1$	63
	$P_2^6(x)$	$x^6 + x^5 + x^4 + x + 1$	
7	$P_1^7(x)$	$x^7 + x^6 + 1$	127
	$P_2^7(x)$	$x^7 + x^4 + 1$	
8	$P_1^8(x)$	$x^8 + x^7 + x^6 + x + 1$	255
	$P_2^8(x)$	$x^8 + x^7 + x^5 + x^3 + 1$	
9	$P_1^9(x)$	$x^9 + x^5 + 1$	511
	$P_2^9(x)$	$x^9 + x^8 + x^7 + x^2 + 1$	
10	$P_1^{10}(x)$	$x^{10} + x^7 + 1$	1023
	$P_2^{10}(x)$	$x^{10} + x^9 + x^8 + x^5 + 1$	
11	$P_1^{11}(x)$	$x^{11} + x^9 + 1$	2047
	$P_2^{11}(x)$	$x^{11} + x^{10} + x^9 + x^7 + 1$	
12	$P_1^{12}(x)$	$x^{12} + x^{11} + x^{10} + x^4 + 1$	4095
	$P_2^{12}(x)$	$x^{12} + x^{11} + x^{10} + x^2 + 1$	

*$P_1^n(x)$ and $P_2^n(x)$ are the generator polynomials of the preferred pair used for obtaining corresponding set of Gold codes of degree n.

At the receiving end, recovered data were compared to the original transmitted data for the determination of BER. Parametric BER graphs were generated for the various code lengths. For the simulations, perfect synchronization and perfect power control were assumed. We do realise that factors such as Doppler effects do affect system performance, but in a fading channel. This study only relates to an AWGNchannel, in which such factors do not apply.

4. RESULTS

This section presents results of simulations that we carried out, starting with the performance for a single user.

4.1 Performance for a single user

We shall start by considering simulation results for a single user, Fig. 1. The right-most curve on this figure is that of uncoded data transmission for a single user. The figure shows the close agreement between analytic and simulation results for the uncoded data transmission. [1]For reference purposes, this curve will be retained on all results to be presented in this paper. The rest of the curves on Fig. 1 show the performance for coded data transmission for different code lengths.

Clearly, Fig. 1 shows that longer Gold codes give better error-rate performance. The figure also shows that the use of Gold codes brings about some coding gain. With reference to uncoded data transmission, at a BER of 10^{-4}, the Gold codes provide coding gain of about 15.6, 21.7, 27.8 and 33.9 dB when N = 31, 127, 511 and 2048 respectively. From this we see that there is a constant 6.1-dB-step in coding gain between adjacent code lengths, which can be explained in terms of the ratio of the process gain of the codes.

It should be noted that the penalty for the coding gain obtained from the use of Gold codes is increase in bandwidth requirements. Each 6 dB improvement in coding gain corresponds to quadrupling of the bandwidth.

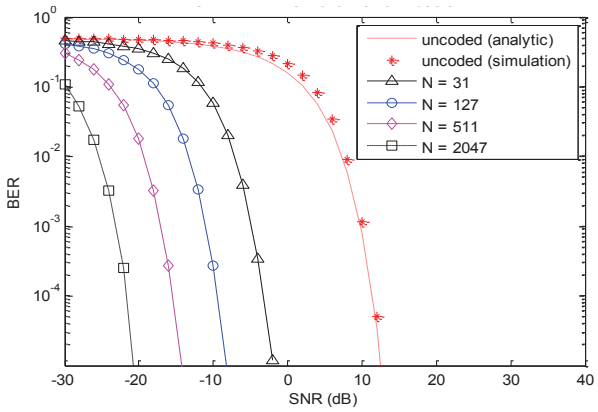

Fig. 1. Bit-error-rate for a single user

[1] An analytic result is obtained by direct implementation of an analytic expression; simulation result is obtained by sending random data through the channel, and then counting the number of bits in error at the receiving end. For the uncoded data transmission, the analytic equation for the BER is: $BER = Q\left(\sqrt{2\left(\frac{E_b}{N_0}\right)}\right)$, where Q is q-function, and E_b/N_0 is bit-energy-per-noise ratio.

4.2 Performance for two to five users

Next, we shall consider the results for a few multiple users. Figs. 2(a) to 2(c) show the BER for two, three and five users respectively. A look at these figures shows that an increase in the number of interferers worsens the system BER. That is, MAI worsens with increasing system load. The results show, for example, that for the code length N = 31 chips, at an SNR of -5 dB, BER is 1.1 x 10^{-3} for a single user, 2.1 x 10^{-2} for two users, 4.9 x 10^{-2} for three users and 1.1 x 10^{-1} for five users. The BERs for the other code lengths (N = 127, 511 and 2047) show a similar trend.

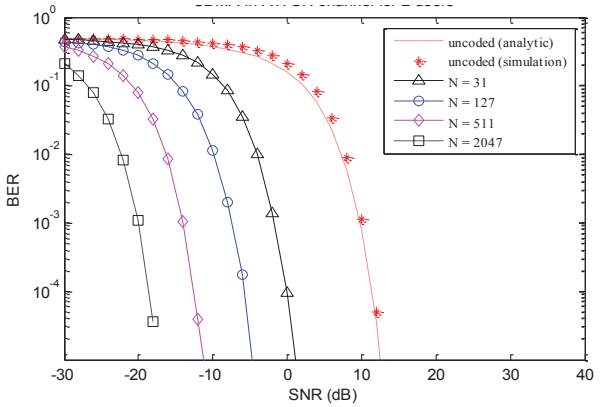

(a)

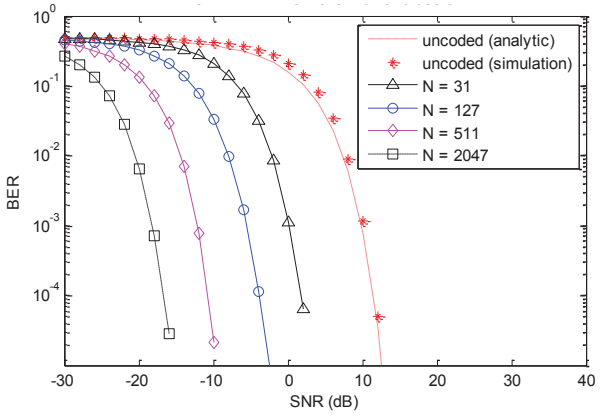

(b)

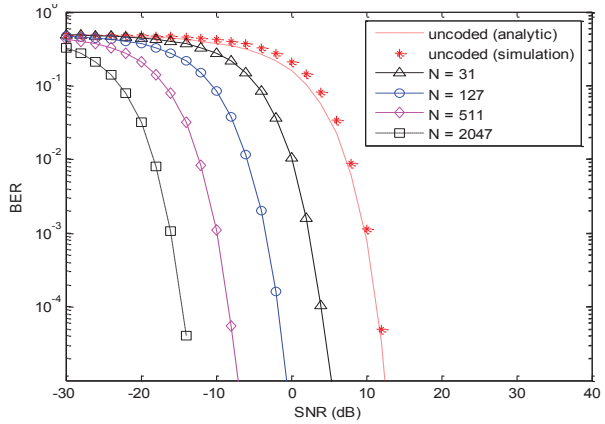

(c)

Fig. 2. Bit-error-rate for (a) two users, (b) three users, and (c) five users.

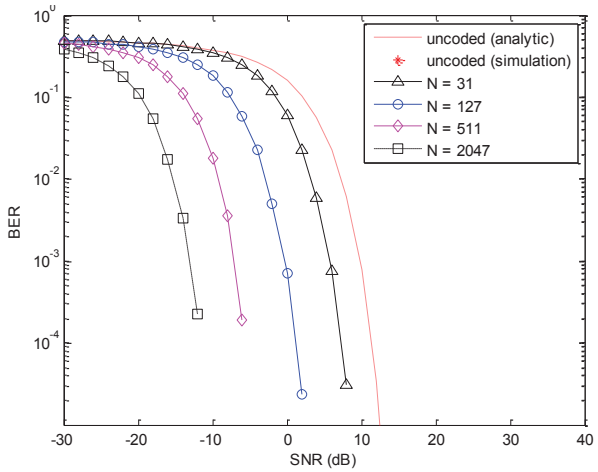

(a)

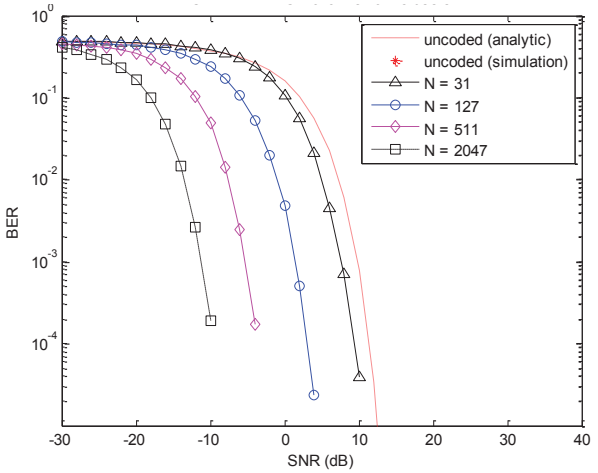

(b)

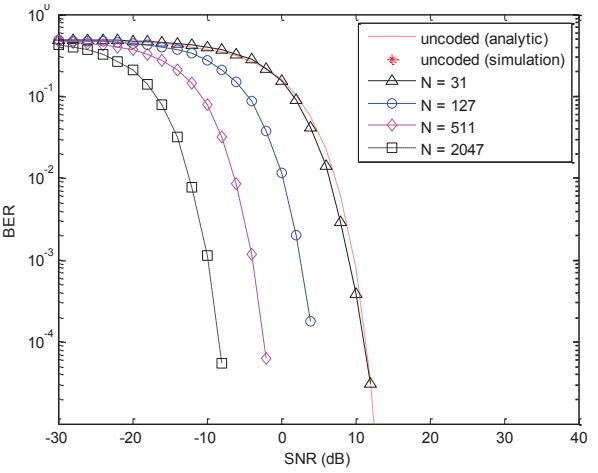

(c)

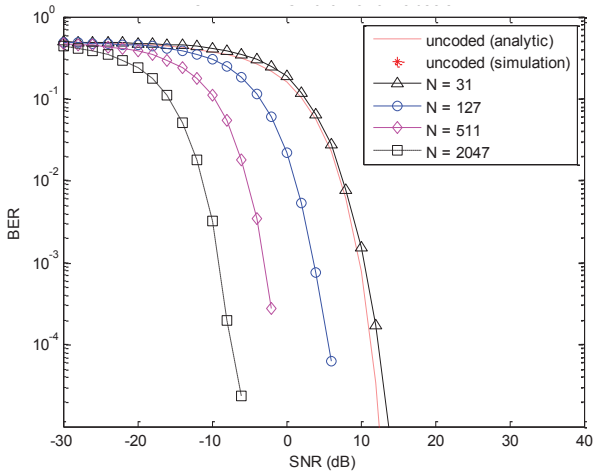

(d)

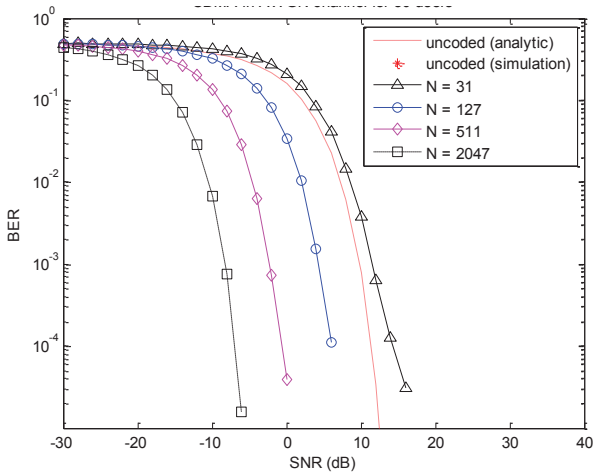

(e)

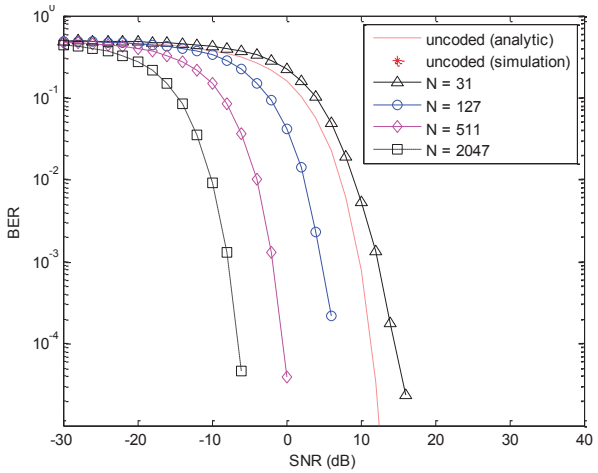

(f)

Fig. 3. Bit-error rate for (a) 10 users, (b) 15 users, (c) 20 users, (d) 25 users, (e) 30 users and (f) 31 users.

4.3 Performance for ten or more users

We shall now consider simulation results for higher numbers of users. Figs. 3(a) to 3(f) show the BER for 10, 15, 20, 25, 30 and 31 users respectively. As with the previous results, these figures show that as the number of users increase, the system BER worsens, resulting from increasing MAI.

For the code length N = 31 chips, for example, the results show that at an SNR of 8 dB, BER is 3.13 x 10^{-4} for ten users, 6.98 x 10^{-4} for 15 users, 2.94 x 10^{-3} for 20 users, 7.71 x 10^{-3} for 25 users, and 1.45 x 10^{-2} for 30 users. Because of the MAI, obtaining the same BER for a system involving a higher number of simultaneous users requires higher SNR. For example, for the 31-chip code, obtaining a BER of 10^{-4} requires an SNR of about -3.27 dB for a single user (Fig. 1), 4.01 dB for five users (Fig. 2c), 7.28 dB for 10 users, 11.07 dB for 20 users and 14.32 dB for 30 users (Figs 3a, c & e).

5. DISCUSSION

The simulation results that have just been presented confirm that as the number of users increases, the system BER worsens. This is consistent with expectation because increasing the number of simultaneous users implies higher MAI. However, a closer look at the results reveals that the simulation results have some surprises, explained as follows.

The simulation results show that as the number of users increase, the system BER degrades at similar rates for all the different code lengths: in general, BER curves for all the code lengths shift together, with all possessing similar slopes at high SNRs (Figs. 2 and 3). In contrast to this, as the number of users increase, system BER is expected to degrade faster for shorter Gold codes. A reason for this is that shorter codes have higher peak cross-correlation coefficients (Table 2). Also, by virtue of their length, shorter codes approach full-load condition earlier than longer codes.

Table 2. Peak cross-correlation of Gold codes*

n	N	t(n)	t(n)/φ(0)
3	7	5	0.7143
4	15	9	0.6000
5	31	9	0.2903
6	63	17	0.2698
7	127	17	0.1339
8	255	33	0.1294
9	511	33	0.0646
10	1023	65	0.0635
11	2047	65	0.0318
12	4095	129	0.0315

*In the last column, peak cross-correlation function, *t(n)*, for Gold code sequence is normalised by peak autocorrelation function *φ(0)*.

Apart from this, for a given code length, BER is expected to increase rapidly as full-load is approached. For example, the BER for a 31-chip Gold code is expected to increase rapidly, to flatten out horizontally, and to exhibit error floor as the number of users approaches 31. In connection with this, the slopes of the BER curves for different code lengths are expected to become increasingly different when the number of users increases. In contrast, the simulation results give no indication of this: even under full load, the 31-chip Gold code does not show any error floor or system saturation.

As a consequence of the difference in rate of degradation of BER with increasing number users, coding gains between BER curves of adjacent code lengths are expected to become increasingly unequal, as opposed to a single-user case, where the coding gain is constant. In contrast to this, the simulation results show no significant difference in coding gain between BERs of adjacent code lengths. The set of curves appears to maintain similar slopes at high SNR, with no visible difference in their coding gain.

The following are explanations for these surprising results:

1. **Selected reference user.** Any set of Gold codes comprises N+2 members. Two of these represent the preferred pair of m-sequences from which the remaining members are derived. In every instance of the current investigation, one of the preferred pairs was used for the encoding (and the decoding) of the data stream of the reference user. Hence, the outcome of the simulation indicates that the preferred pair has low cross-correlation with the rest of the code set.
2. **Peak correlation coefficient.** Peak correlation coefficient (Table 1) only gives the peak value that the correlation function (Equation 9) of a Gold code could have, but not the frequency of occurrence or the distribution of the peaks. If the peak value happens to be few and sparsely distributed for a particular code set, its degrading effect on MAI may not be very significant.
3. **Bipolarity of Gold codes.** Gold codes are bipolar codes, being +1 at one instant, and -1 at another. The same fact applies to the cross-correlation coefficients of the codes. As a result, there is the possibility of interference from one user cancelling out that of another. If a code set happens to be well-behaved, the mutual cancelling of the inteference from offending users might turn out to enhance the system BER performance.
4. **Synchronisation.** For the work reported in this paper, perfect synchronisation was assumed, and this might be a factor.

At first sight, the absence of error floor, even when the system was heavily loaded, raises a question on the validity of the simulation results. Regarding this, further investigation reveals that the outstanding performance is peculiar to the sets of Gold codes that have just been considered in this paper. Additional simulation results show that some other sets of Gold codes lack such excellent performance. Fig. 4 shows examples of these. Looking at this figure, it is clear that the BER performance of this category of codes has error floor when

the system is significantly loaded. Results show that this inferior behaviour is peculiar to even-degree codes. These results indicate the need for careful choice of spreading codes when designing a CDMA system.

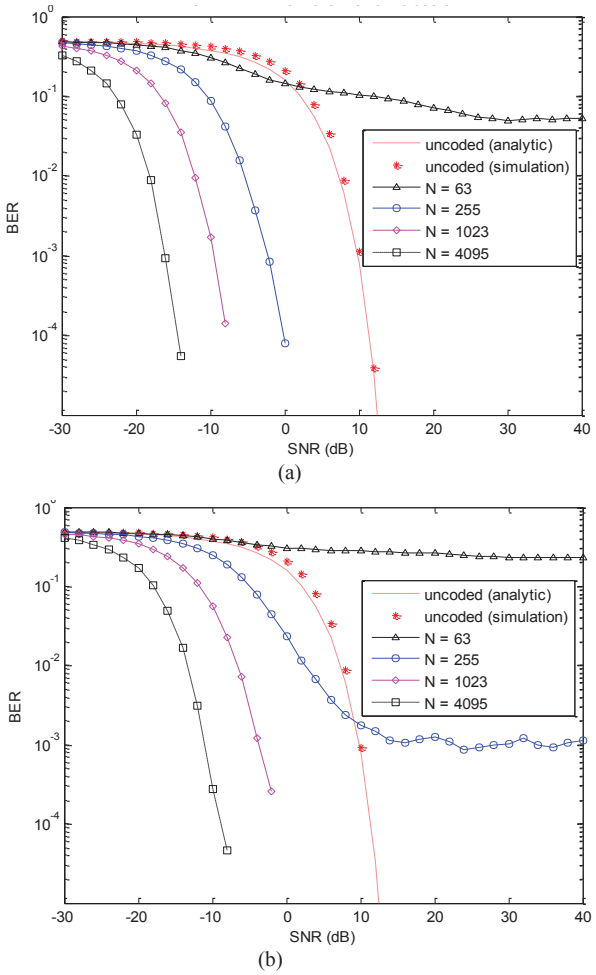

Fig. 4. Samples of results showing inferior performance of some other sets of Gold codes for (a) 10 users and (b) 30 users. These codes exhibited error floor and system saturation when the system was significantly loaded.

6. FUTURE WORK

The work reported in this paper involved the use of odd-degree Gold codes. As an extension of this, an effort is being made to investigate the system performance for even-degree Gold codes.

Apart from this, this paper considered the system performance in an AWGN channel. In the future, the system performance in a frequency-selective channel shall be investigated. This would entail the modelling of the performance of a multi-user, multi-carrier CDMA system in a frequency-selective channel.

This paper also assumed perfect synchronisation, which is only possible in the downlink. The system performance in an asynchronous environment might be considered in the future.

7. CONCLUSION

In this paper, we studied the performance of certain sets of Gold codes in a multi-user DS-CDMA system. Using simulation results, we examined the system BER performance under increasing system load for different code lengths. The sets of Gold codes performed significantly better than expected, with no indication of error floor or system saturation even when the system was heavily loaded. The outcome of this work indicates that the sets of Gold codes have better cross-correlation properties that make them more suitable for use in multi-user CDMA systems. The results also suggest that certain important properties of Gold codes are yet to be discovered.

AKNOWLEDGEMENT

The authors wish to express gratitude to the German Academic Exchange Programme (DAAD - Deutscher Akademischer Austausch Dienst), as well as the Centre of Excellence (CoE), and the Centre for Engineering Postgraduate Studies (CEPS), both of the School of Engineering, University of KwaZulu-Natal, for supporting this research work.

REFERENCES

[1] P. Samundiswary and P. V. Kalyan: "Performance Analysis of WCDMA using Different Spreading Codes," *International Journal of Computer Applications,* vol. 38, pp. 8-11, 2012.

[2] Z. Gu, S. Xie, S. Rahardja, E. T. Sze, and Y. Xin: "Performance Comparison of Spreading Sequences in Synchronous MC-CDMA Systems," in *Information, Communications and Signal Processing, 2005 Fifth International Conference* , 2005, pp. 633-637.

[3] R. Liu, E. G. Chester, and B. S. Sharif: "Performance of asynchronous multicarrier CDMA multiuser receiver over frequency selective multipath fading channels," *Electronics Letters,* vol. 40, pp. 48-49, 2004.

[4] C. Hsiao-Hwa and C. Hsin-Wei: "Generation of perfect orthogonal complementary codes for their applications in interference-free CDMA systems," in *Personal, Indoor and Mobile Radio Communications, 2004. PIMRC 2004. 15th IEEE International Symposium on*, 2004, pp. 734-738 .

[5] C. Hsiao-Hwa and C. Hsin-Wei: "Design of perfect complementary codes to implement interference-free CDMA systems," in *Global Telecommunications Conference, 2004. GLOBECOM '04. IEEE*, 2004, pp. 1096-1100 .

[6] C. Hsiao-Hwa and C. Hsin-Wei: "Generation of superset of perfect complementary codes for next generation CDMA systems," in *Military Communications Conference, 2004. MILCOM 2004. 2004 IEEE*, 2004, pp. 14-20 .

[7] C. Hsiao-Hwa, C. Hsin-Wei, and M. Guizani: "Orthogonal complementary codes for interference-

free CDMA technologies," *Wireless Communications, IEEE,* vol. 13, pp. 68-79, 2006.

[8] C. Hsiao-Hwa, C. Shin-Wei, and M. Guizani: "On Next Generation CDMA Technologies: The REAL Approach for Perfect Orthogonal Code Generation," *Vehicular Technology, IEEE Transactions on,* vol. 57, pp. 2822-2833, 2008.

[9] J. Li, H. Aiping, M. Guizani, and C. Hsiao-Hwa: "Inter-Group Complementary Codes for Interference-Resistant CDMA Wireless Communications," *Wireless Communications, IEEE Transactions on,* vol. 7, pp. 166-174, 2008.

[10] M. Wei-Xiao, S. Si-Yue, C. Hsiao-Hwa, and L. Jin-Qiang: "Multi-User Interference Cancellation in Complementary Coded CDMA with Diversity Gain," *Wireless Communications Letters, IEEE,* vol. 2, pp. 303-306, 2013.

[11] M. Pal and S. Chattopadhyay: "A novel orthogonal minimum cross-correlation spreading code in CDMA system," in *Emerging Trends in Robotics and Communication Technologies (INTERACT), 2010 International Conference on*, 2010, pp. 80-84.

[12] R. C. Dixon: *Spread Spectrum Systems: CDMA Design and Capabilities*: Wiley John & Sons, 2009.

[13] C. Sung-Tai and N. Jong-Seon: "On the cross-correlation distributions between p-ary m-sequences and their decimated sequences," in *Signal Design and its Applications in Communications (IWSDA), 2011 Fifth International Workshop on*, 2011, pp. 4-4.

[14] A. Ziani and A. Medouri: "Analysis of different Pseudo-Random and orthogonal spreading sequences in DS-CDMA," in *Multimedia Computing and Systems (ICMCS), 2012 International Conference on*, 2012, pp. 558-564.

[15] M. B. Mollah and M. R. Islam: "Comparative analysis of Gold Codes with PN codes using correlation property in CDMA technology," in *Computer Communication and Informatics (ICCCI), 2012 International Conference* , 2012, pp. 1-6.

[16] L. Tao and X. H. Chen: "Comparison of correlation parameters of binary codes for DS/CDMA systems," in *Singapore ICCS '94. Conference Proceedings.*, 1994, pp. 1059-1063 .

[17] K. H. A. Karkkainen and P. A. Leppanen: "Comparison of the performance of some linear spreading code families for asynchronous DS/SSMA systems," in *Military Communications Conference, 1991. MILCOM '91, Conference Record, Military Communications in a Changing World., IEEE*, 1991, pp. 784-790 .

[18] T. M. Nazmul Huda and S. F. Islam: "Correlation analysis of the gold codes and walsh codes in CDMA technology," in *Internet, 2009. AH-ICI 2009. First Asian Himalayas International Conference on*, 2009, pp. 1-4.

[19] M. Cinteza, I. Marghescu, and T. Radulescu: "Design of PN Sequence Families with Bounded Correlation Properties, Using Genetic Algorithms," in *Computer as a Tool, 2005. EUROCON 2005.The International Conference* , 2005, pp. 1818-1821.

[20] M. Gouda, A. El-Hennawy, and A. E. Mohamed: "Detection of Gold Codes Using Higher-Order Statistics," in *Informatics and Computational Intelligence (ICI), 2011 First International Conference on*, 2011, pp. 361-364.

[21] M. Akhavan-Bahabdi and M. Shiva: "Double orthogonal codes for increasing capacity in MC-CDMA systems," in *Wireless and Optical Communications Networks, 2005. WOCN 2005. Second IFIP International Conference* , 2005, pp. 468-471.

[22] D. Kedia, M. Duhan, and S. L. Maskara: "Evaluation of correlation properties of Orthogonal spreading codes for CDMA wireless mobile communication," in *Advance Computing Conference (IACC), 2010 IEEE 2nd International*, 2010, pp. 325-330.

[23] K. Khoongming, G. Guang, and D. R. Stinson: "A new family of Gold-like sequences," in *Information Theory, 2002. Proceedings. 2002 IEEE International Symposium* , 2002, p. 181.

[24] Z. Yang, L. Guangxia, and H. Jing: "On the BER performance simulation of LASCDMA," in *World Automation Congress (WAC), 2012*, 2012, pp. 1-3.

[25] G. Suchitra and M. L. Valarmathi: "Performance of Concatenated Complete Complementary code in CDMA systems," in *Cognitive Wireless Systems (UKIWCWS), 2009 First UK-India International Workshop* , 2009, pp. 1-5.

[26] V. V. Barinov, V. S. Kuznetsov, and M. V. Lebedev: "Spreading ensembles with improved correlation properties for multiple access," in *Personal, Indoor and Mobile Radio Communications, 2005. PIMRC 2005. IEEE 16th International Symposium on*, 2005, pp. 1081-1085 .

[27] J. Bi, Y. Wang, H. Tian, and K. Yi: "A new method to design CDMA spreading sequences," in *Communication Technology Proceedings, 2000. WCC - ICCT 2000. International Conference on*, 2000, pp. 526-529.

[28] R. Gold: "Characteristic Linear Sequences and Their Coset Functions," *SIAM Journal on Applied Mathematics,* vol. 14, pp. 980-985, 1966.

[29] R. Gold: "Optimal binary sequences for spread spectrum multiplexing (Corresp.)," *Information Theory, IEEE Transactions on,* vol. 13, pp. 619-621, 1967.

[30] R. Gold: "Maximal recursive sequences with 3-valued recursive cross-correlation functions (Corresp.)," *Information Theory, IEEE Transactions on,* vol. 14, pp. 154-156, 1968.

GENERAL FAULT ADMITTANCE METHOD SOLUTION OF A LINE-TO-GROUND FAULT

J.D. Sakala* and J.S.J. Daka**

** Faculty of Engineering and Technology, Dept. of Electrical Engineering, University of Botswana, 4775 Notwane Road, Private Bag 0022, Botswana, E-mail: sakala@mopipi.ub.bw*
*** Faculty of Engineering and Technology, Dept. of Electrical Engineering, University of Botswana, 4775 Notwane Road, Private Bag 0022, Botswana, E-mail: dakajsj@mopipi.ub.bw*

Abstract: Line-to-ground faults are usually analysed using symmetrical components. For this type of fault the sequence networks are connected in series and solved to obtain the sequence currents and voltages at the fault point. These are then used to determine the symmetrical component voltages at the other bus bars and the symmetrical component currents in the lines. The phase quantities are obtained by transformation. In this approach, the connection of the sequence networks must be known for the fault. In contrast, the solution by the general method of fault admittance matrix does not require prior knowledge of how the sequence networks are connected. It is therefore more versatile than the classical methods. It does however require the fault admittance matrix at the fault point. For a line-to-ground fault, of zero impedance, the fault admittance matrix is infinite and has to be simulated. The paper presents a procedure for simulating the short circuit, a requirement for using the general fault admittance method. The results obtained are as accurate as those obtained using the classical approaches.

Key words: Unbalanced faults analysis, Line-to-ground fault, Fault admittance matrix, short circuit simulation, delta earthed-star transformer.

1. INTRODUCTION

The paper presents a method for solving the single line-to-ground fault using the general fault admittance method. The method differs from the classical approaches based on symmetrical components since it does not require prior knowledge of the relationships of sequence components currents and voltages, and the interconnection of the sequence networks. However, the method requires formulation of the fault admittance matrix at the fault point, for finding the sequence currents and voltages at the fault and in the network. The line-to-ground short circuit fault has zero impedances in the faulted phase and ground path, which have infinite admittances.

Sakala and Daka have used the general fault admittance method to solve various faults [1-8]. They have however not presented a detailed simulation of the line-to-ground fault. This paper discusses a procedure for simulating the zero impedance for the line-to-ground short circuit.

2. BACKGROUND

2.1 Line-to-ground Fault Interconnection of Sequence Networks

The positive, negative and zero sequence currents for the line-to-ground fault are equal while the positive, negative and zero sequence voltages summate to zero. The sequence networks are therefore connected in series and the sequence currents and voltages at the fault point are determined. The symmetrical component currents and voltages in the rest of the network are then calculated. Phase currents and voltages are found by transforming the respective symmetrical component values [9-14].

2.2 General Fault Representation

A single line-to-ground fault presents a low value impedance, with zero value for a direct short circuit or metallic fault, to one of the phases at the point of fault in the network. In general, a fault may be represented as shown in Figure 1.

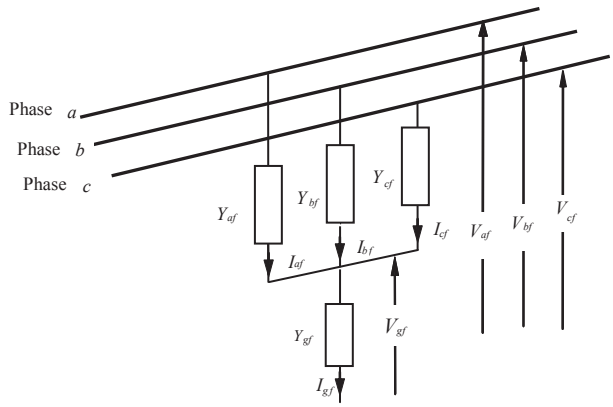

Figure 1: General Fault Representation [8]

In Figure 1, a fault at a bus bar is represented by fault admittances in each phase, and the admittance in the ground path. Note that the fault admittance for a short-circuited phase is represented by an infinite value, while that for an open-circuited phase is a zero value. Thus for

a line-to-ground fault the admittances Y_{bf} and Y_{cf} are zero while those for Y_{af} and Y_{gf} are infinite.

A systematic approach for using the general fault admittance method is given by Sakala and Daka [8]. The equations and procedures for a line-to-ground fault are summarized in this paper to give the reader a comprehensive view of the methodology.

2.3 Summary of General Fault Admittance Method for Line-to-Ground Fault

The general fault admittance matrix is given by

$$Y_f = \left(\frac{1}{Y_{af}+Y_{bf}+Y_{cf}+Y_{gf}}\right) \times \begin{bmatrix} Y_{af}\left(Y_{bf}+Y_{cf}+Y_{gf}\right) & -Y_{af}Y_{bf} & -Y_{af}Y_{cf} \\ -Y_{af}Y_{bf} & Y_{bf}\left(Y_{af}+Y_{cf}+Y_{gf}\right) & -Y_{bf}Y_{cf} \\ -Y_{af}Y_{cf} & -Y_{bf}Y_{cf} & Y_{cf}\left(Y_{af}+Y_{bf}+Y_{gf}\right) \end{bmatrix} \quad (1)$$

Equation (1) is transformed using the symmetrical component transformation matrix be T, and its inverse be T^{-1}, where

$$T = \begin{bmatrix} 1 & 1 & 1 \\ \alpha^2 & \alpha & 1 \\ \alpha & \alpha^2 & 1 \end{bmatrix} \quad \text{and} \quad T^{-1} = \frac{1}{3}\begin{bmatrix} 1 & \alpha & \alpha^2 \\ 1 & \alpha^2 & \alpha \\ 1 & 1 & 1 \end{bmatrix},$$

in which $\alpha = 1\angle 120°$ is a complex operator.

The symmetrical component fault admittance matrix is given by the product

$$Y_{fs} = T^{-1}Y_f T$$

The general expression [8] for Y_{fs} is given by:

$$Y_{fs} = \frac{1}{Y_{af}+Y_{bf}+Y_{cf}+Y_{gf}}\begin{bmatrix} Y_{fs11} & Y_{fs12} & Y_{fs13} \\ Y_{fs21} & Y_{fs22} & Y_{fs23} \\ Y_{fs31} & Y_{fs32} & Y_{fs33} \end{bmatrix} \quad (2)$$

where

$$Y_{fs11} = Y_{fs22} = \frac{1}{3}Y_{gf}\left(Y_{af}+Y_{bf}+Y_{cf}\right)+Y_{af}Y_{bf}+Y_{af}Y_{cf}+Y_{bf}Y_{cf}$$

$$Y_{fs33} = \frac{1}{3}Y_{gf}\left(Y_{af}+Y_{bf}+Y_{cf}\right)$$

$$Y_{fs12} = \frac{1}{3}Y_{gf}\left(Y_{af}+\alpha^2 Y_{bf}+\alpha Y_{cf}\right)-\left(Y_{bf}Y_{cf}+\alpha Y_{af}Y_{bf}+\alpha^2 Y_{af}Y_{cf}\right)$$

$$Y_{fs21} = \frac{1}{3}Y_{gf}\left(Y_{af}+\alpha Y_{bf}+\alpha^2 Y_{cf}\right)-\left(Y_{bf}Y_{cf}+\alpha^2 Y_{af}Y_{bf}+\alpha Y_{af}Y_{cf}\right)$$

$$Y_{fs13} = Y_{fs32} = \frac{1}{3}Y_{gf}\left(Y_{af}+\alpha Y_{bf}+\alpha^2 Y_{cf}\right) \quad \text{and}$$

$$Y_{fs31} = Y_{fs23} = \frac{1}{3}Y_{gf}\left(Y_{af}+\alpha^2 Y_{bf}+\alpha Y_{cf}\right)$$

For a line-to-ground fault:

$Y_{af} = Y,\quad Y_{bf} = Y_{cf} = 0,\quad Y_{gf} = \infty$ i.e. $Z_{gf} = 0$

$$Y_{fs} = \frac{YY_{gf}}{3\left(Y+Y_{gf}\right)}\begin{bmatrix} 1 & 1 & 1 \\ 1 & 1 & 1 \\ 1 & 1 & 1 \end{bmatrix} = \frac{Y}{3}\begin{bmatrix} 1 & 1 & 1 \\ 1 & 1 & 1 \\ 1 & 1 & 1 \end{bmatrix} \quad (3)$$

Note that when Y is infinite the analysis is performed by a limit study, either by substituting Y_{fs} in the expression for the symmetrical component fault currents or by choosing a small fault impedance that gives an accurate result when Y_{fs} is used in the general form of the solution.

Currents in the Fault: At the faulted bus bar, say j, the symmetrical component currents in the fault, for any fault, are in the general form of the solution given by

$$I_{fsj} = Y_{fs}\left(U + Z_{sjj}Y_{fs}\right)^{-1}V_{sj}^{\ 0} \quad (4)$$

where U is the unit matrix

$$U = \begin{bmatrix} 1 & 0 & 0 \\ 0 & 1 & 0 \\ 0 & 0 & 1 \end{bmatrix}$$

and Z_{sjj} is the jj^{th} component of the symmetrical component bus impedance matrix Z_s.

$$Z_{sjj} = \begin{bmatrix} Z_{sjj+} & 0 & 0 \\ 0 & Z_{sjj-} & 0 \\ 0 & 0 & Z_{sjj0} \end{bmatrix}$$

Where the elements Z_{sjj+}, Z_{sjj-}, and Z_{sjj0} are the Thevenin's positive, negative and zero sequence impedances at the faulted bus bar. Note that as the network is balanced the mutual terms are all zero.

The sequence bus impedance matrix Z_s may be obtained by inverting the sequence bus admittance matrix Y_s or by directly assembly from the impedances of the network components.

In equation (4) $V_{sj}^{\ 0}$ is the prefault symmetrical component voltage at the faulted bus bar j.

$$V_{sj}^{\ 0} = \begin{bmatrix} V_{sj+} \\ V_{sj-} \\ V_{sj0} \end{bmatrix} = \begin{bmatrix} V_+ \\ 0 \\ 0 \end{bmatrix}$$

where V_+ is the positive sequence voltage before the fault. The negative and zero sequence voltages are zero because the system is balanced prior to the fault.

The symmetrical component fault admittance matrix in equation (3) may be substituted in equation (4) to obtain

the simplified value of I_{fsj} given in equation (4a), in which V_j^0 is the prefault voltage on bus bar j.

$$I_{fsj} = V_j^0 \frac{\frac{Y}{3}}{1+\left(\frac{Y}{3}\right)\left(Z_{sjj+}+Z_{sjj-}+Z_{sjj0}\right)}\begin{bmatrix}1\\1\\1\end{bmatrix} = V_j^0 \frac{1}{\left(\frac{3}{Y}\right)+\left(Z_{sjj+}+Z_{sjj-}+Z_{sjj0}\right)}\begin{bmatrix}1\\1\\1\end{bmatrix} \quad (4a)$$

The simplified formulation in equation (4a) is useful for checking the accuracy of the symmetrical component currents in the fault when the general form of the solution is used.

The phase currents in the fault are then obtained by transformation

$$I_{fpj} = \begin{bmatrix}I_{afj}\\I_{bfj}\\I_{cfj}\end{bmatrix} = TI_{fsj} \quad (5)$$

Voltages at the Bus bars: The symmetrical component voltage at the faulted bus bar j is given by

$$V_{fsj} = \begin{bmatrix}V_{j+}\\V_{j-}\\V_{j0}\end{bmatrix} = \left(U + Z_{sjj}Y_{fs}\right)^{-1}V_{sj}{}^{0} \quad (6)$$

The symmetrical component voltage at a bus bar i for a fault at bus bar j is given by:

$$V_{fsi} = \begin{bmatrix}V_{i+}\\V_{i-}\\V_{i0}\end{bmatrix} = V_{si}{}^{0} - Z_{sij}Y_{fs}\left(U + Z_{sjj}Y_{fs}\right)^{-1}V_{sj}{}^{0} \quad (7)$$

where $V_{si}{}^{0} = \begin{bmatrix}V_{i+}{}^{0}\\0\\0\end{bmatrix}$

are the symmetrical component prefault voltages at bus bar i. Note that the negative and zero sequence prefault voltages are zero.

In equation (7), Z_{sij} is the ij^{th} components of the symmetrical component bus impedance matrix, the mutual terms for row i and column j (corresponding to bus bars i and j)

$$Z_{sij} = \begin{bmatrix}Z_{sij+} & 0 & 0\\0 & Z_{sij-} & 0\\0 & 0 & Z_{sij0}\end{bmatrix}$$

The phase voltages in the fault, at bus bar j, and at bus bar i are then obtained by transformation

$$V_{fpj} = \begin{bmatrix}V_{afi}\\V_{bfi}\\V_{cfi}\end{bmatrix} = TV_{fsj} \text{ and } V_{fpi} = \begin{bmatrix}V_{afpi}\\V_{bfpi}\\V_{cfpi}\end{bmatrix} = TV_{fpi} \quad (8)$$

Currents in Lines and Generators: The symmetrical component currents in a line between bus bars i and j is given by

$$I_{fsij} = Y_{fsij}\left(V_{fsi} - V_{fsj}\right) \quad (9)$$

where

$$Y_{fsij} = \begin{bmatrix}Y_{fsij+} & 0 & 0\\0 & Y_{fsij-} & 0\\0 & 0 & Y_{fsij0}\end{bmatrix}$$

is the symmetrical component admittance of the branch between bus bars i and j.

The same equation applies to a generator where the source voltage is the prefault induced voltage and the receiving end bus bar voltage is the postfault voltage at the bus bar.

The phase currents in the branch ij are found by transformation

$$I_{fpij} = \begin{bmatrix}I_{aifj}\\I_{bifj}\\I_{cfij}\end{bmatrix} = TI_{fsij} \quad (10)$$

2.4 Load Current Considerations

In practice faults occur on power systems that are supplying loads. The load conditions are solved in a load flow analysis and the results form the basis for a fault analysis. Usually the post fault currents are a superimposition of the load currents and the currents due to the fault [9-14].

There are some characteristic differences between load and fault currents. The magnitudes of the load currents are usually either equal to, or below, the rated values for the particular parts of the power system, and their phase angles give large active components. In contrast, the magnitudes of the fault currents are usually much larger that the rated values with phase angles that are in quadrature to the voltages. The explanations are that fault impedances are usually much smaller than load impedances and the impedances of the components of a faulted power system are predominantly reactive [9-14].

In a fault analysis the following assumptions are usually made:

a) Transformers are represented by their leakage reactance.

b) Transmission lines are represented by their series reactance.
c) Synchronous machines are modelled as constant voltages behind direct axis sub-transient reactance.
d) Non-spinning loads are ignored.
e) Induction motors are either ignored, or treated as synchronous motors.
f) Pre-fault voltages are assumed to be 1.0 per unit [11].

In the superposition approach the fault currents are found independently of the load currents and then added to the former. In this work, which considers the simulation of a line-to-ground short circuit, it is acceptable to neglect the load currents as their values does not affect the solution of the fault currents due to the fault.

2.5 Delta-star Transformer Line-To-Ground Fault Current

To validate the method a simple sample power system with a delta-star connected transformer feeding a transmission line on which a line-to-ground fault occurs at its far end is used. The inclusion of a delta-star connected transformer necessitated inclusion of a phase shifting routine in the computer program.

The voltages of a delta-star connected transformer with a 30° phase shift between the delta and star connected sides are shown in Figure 2. Note that the phase ***a*** voltage on the star side in phase ***a*** is in phase with the voltage V_{ac} that is between the ***a*** and ***c*** phases on the delta connected side. The equivalent phase ***a*** voltage on the delta-connected side leads the equivalent phase ***a*** voltage on the star-connected side.

The winding connections for such a transformer are shown in Figure 3, which also shows quantitatively the per unit currents which would flow for a line-to-ground fault on phase ***a*** beyond the star-connected side of the transformer. The fault current I_f only flows in phase ***A*** winding on the star-connected side and in phase **a** winding on the delta-connected side. However due to the connections on the delta side the currents appear in the ***a*** and ***c*** phases on the supply side of the delta-connected side. Therefore the line-to-ground fault on the star-connected side appears as a line-to-line fault on the supply side of the delta-connected side.

The phase shifts of the delta earthed-star transformer are included in its model so that the sequence voltages and currents have the appropriate angles.

2.4 Power System Size Considerations

One of the issues considered in this work was the size of system to be studied. In particular whether the size affects the effectiveness and application of the general fault admittance method. A pertinent factor is that in computation work the size of a power system being studied has a bearing on the memory requirements of the computer being used.

It is shown in the section 2.3 that the general fault admittance method uses the sequence impedance matrix Z_{sjj} at the faulted bus bar. This matrix is used to compute the sequence fault currents at the faulted bus bar using Equation (4), which are then used to calculate the sequence voltages at the other bus bars using Equation (7). In effect Z_{sjj} gives the Thevenin's sequence impedance at the faulted bus bar. This is the equivalent sequence impedances as seen from the faulted bus bar looking into the network. In effect the network is reduced to its Thevenin's equivalent circuit, irrespective of size.

The size of the network therefore has no effect on whether the general fault admittance method works or not. What is important is that the sequence bus impedance matrix of the system being studied, of size $3n \times 3n$, can be assembled/calculated. Once the matrix is obtained, the values at the faulted bus bar are used to calculate the sequence fault currents. It was therefore decided to study a simple system, which simplifies validation of the method.

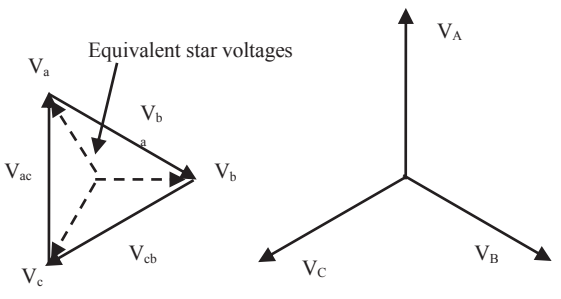

Figure 2: Delta star Transformer Voltages for Yd11[7]

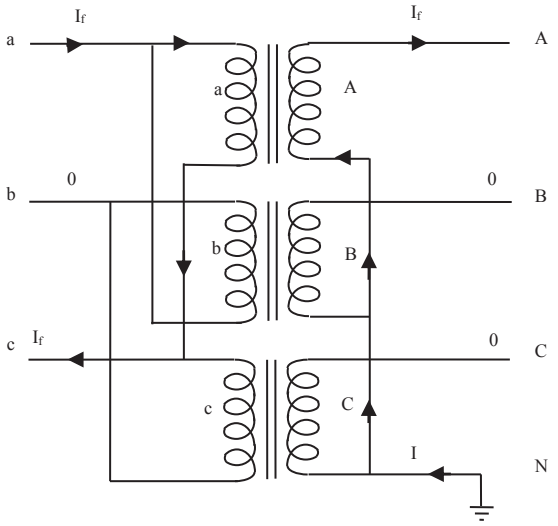

Figure 3: Transformer Currents for a Line-to-Ground Fault

3. LINE-TO-GROUND FAULT SIMULATION

3.1 Zero Impedance Representation

The impedances required to simulate the line-to-ground fault in general terms are the impedance in the faulted phase and the ground path. In the current work various impedances were considered, namely; purely resistive, resistive and inductive and purely inductive. The impedances in the faulted phase and ground have been assumed equal. In practice, this is not significant as the two values are added to arrive at the total impedance in the ground path.

Equation (3) gives the symmetrical component fault admittance matrix for a line-to-ground fault. It is restated here for easy of reference:

$$Y_{fs} = \frac{YY_{gf}}{3\left(Y + Y_{gf}\right)}\begin{bmatrix}1 & 1 & 1\\ 1 & 1 & 1\\ 1 & 1 & 1\end{bmatrix} = \frac{Y}{3}\begin{bmatrix}1 & 1 & 1\\ 1 & 1 & 1\\ 1 & 1 & 1\end{bmatrix}$$

The value Y is the fault admittance in the faulted phase with the ground assumed to be a metallic contact, with $Z_{gf} = 0$. When the phase fault impedance is zero then Y is infinite and the general form solution breaks down.

3.2 Short Circuit Simulation Details

The procedure for simulating short circuits is summarized in Figure 4. The value of the fault impedance is initially assumed to be a very small value, such as 10^{-3} Ω, much smaller than the value of the Thevenin's positive sequence impedance at the faulted bus bar. The sequence currents are calculated using the small value.

Next the fault impedance is reduced by a factor, such as 10^{-1}, and the sequence currents re-calculated. The magnitude of the change in the positive sequence fault current is compared against a pre-determined tolerance, such as 10^{-8}.

If, or when, the absolute value of the change is smaller than the tolerance, the solution is considered to have converged, otherwise the impedance is reduced further and the sequence fault currents calculated again and the resulting change checked for convergence.

The procedure is repeated until convergence, or until the specified maximum number of iterations, which could be say 15, are reached and the solution is considered not to have converged.

3.3 Computation of the Line-to-ground Fault

A computer program has been developed, based on the equations (1) to (10), to solve unbalanced faults on a general power system using the fault admittance matrix method. The program is applied on a simple power system comprising of three bus bars to solve for a line-to-ground fault. A simple system is chosen because it is easy to check the results against those that are obtained by hand. Once the program is validated on a simple system then it can be used on large practical systems.

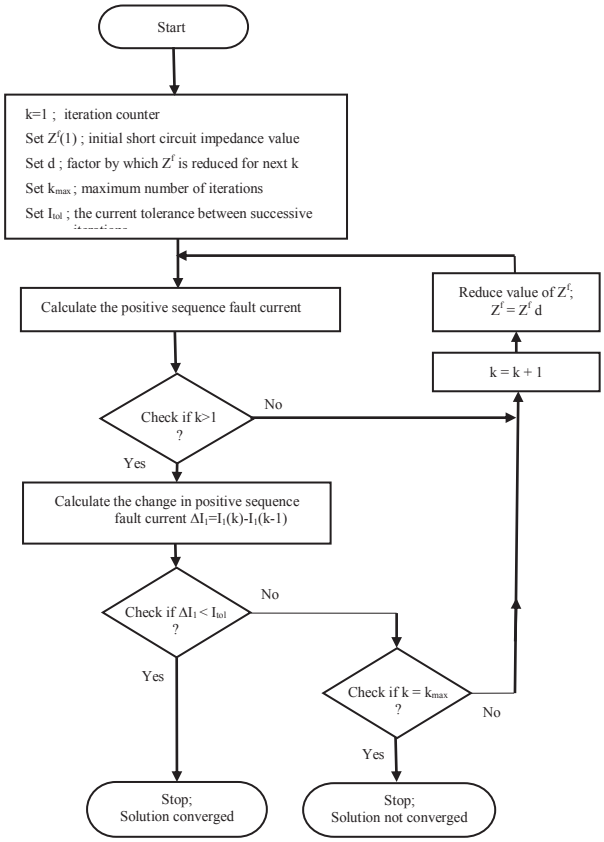

Figure 4: Fault Impedance Simulation Procedure

3.4 Sample System

Figure 5 shows a simple three bus bar power system with one generator, one transformer and one transmission line. The system is configured based on the simple power system that Saadat uses [10].

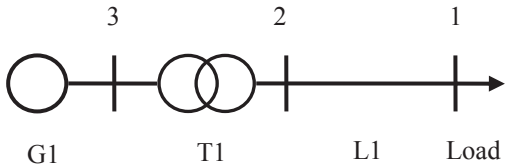

Figure 5: Sample Three Bus Bar System

The power system per unit data is given in Table 1, where the subscripts *1*, *2*, and *0* refer to the positive, negative and zero sequence values respectively. The neutral point of the generator is grounded through a zero impedance.

The transformer windings are delta connected on the low voltage side and earthed-star connected on the high voltage side, with the neutral solidly grounded. The phase shift of the transformer is *30°*, i.e. from the generator side to the line side. Figure 2 shows the relationship of transformer voltages for a delta star transformer connection Yd11 that has a *30°* phase shift.

The network sequence admittance and impedance matrices are calculated and assembled in the computer program. In particular the sequence bus impedance matrix has 3*n* rows and 3*n* columns where *n* is the number of bus bars.

It is assumed (Section 2.4), that the power system is not on load before the occurrence of a fault and therefore the pre-fault voltages are *1.0* per unit at the bus bars and in the generator.

The line-to-ground fault occurs at bus bar *1*, the load bus bar. Various impedances to simulate the line-to-ground fault are considered; purely resistive, a resistive and inductive combination, and a purely inductive value.

The line-to-ground fault is described by the impedances in the respective phases and in the ground path. For the line-to-ground fault the impedances are in the faulted phase, usually *a* phase, and the ground path. The open circuit values for the healthy phases, usually the *b* and *c* phases, need not be input since their respective fault admittances are zero.

4. RESULTS AND DISCUSSIONS

4.1 Fault Simulation Impedances

The values of fault impedances that give accurate values of sequence currents, i.e. to the specified tolerance of the positive sequence currents, are given in Table 2(a).

Case 1 in the table is for a purely resistive fault, case 2 is for a resistive and inductive fault while case 3 is for a purely inductive fault. The purely resistive fault impedances give a better convergence, large fault impedance values, than for the other two cases.

There is a limit as to how low the fault impedance should be. When the value becomes too low the matrix $(U+Z_{sjj}Y_{fs})^{-1}$ in equation (6) does not compute, and the solution for the symmetrical component currents breaks down. Before the solution breaks down the values of the symmetrical component currents become inaccurate, depending on how much of the effect of the unity matrix in the equation is lost. Table 2(b) gives the lowest values of the fault impedances and the corresponding positive sequence current tolerances and current differences. Note that for the purely inductive fault impedances the values of 5×10^{-10} gave zero current difference, and hence, convergence of the solution. Consequently lower values of purely inductive fault impedances could not be use.

Table 1: Power System Data

Item	S_{base} (MVA)	V_{base} (kV)	X_1 (pu)	X_2 (pu)	X_0 (pu)
G_1	100	20	0.15	0.15	0.05
T_1	100	20/220	0.1	0.1	0.1
L_1	100	220	0.25	0.25	0.7125

Table 2(a): Solution Convergence Characteristics

Fault impedance			Current tolerance	Current difference
Case	Phase a	Ground path		
1 (r+j0)	5×10^{-6}	5×10^{-6}	1×10^{-8}	7.5×10^{-9}
2 (r+jx)	$(5+j5)\ 10^{-10}$	$(5+j5)\ 10^{-10}$	$1x10^{-8}$	-9.3×10^{-10}
3 (0+jx)	$j5\times10^{-10}$	$j5\times10^{-10}$	1×10^{-8}	0

Table 2(b): Lowest Fault Impedances

Fault impedance			Current tolerance	Current difference
Case	Phase a	Ground path		
1 (r+j0)	5×10^{-9}	5×10^{-9}	1×10^{-14}	7.5×10^{-15}
2 (r+jx)	$(5+j5)\ 10^{-10}$	$(5+j5)\ 10^{-10}$	1×10^{-9}	-9.3×10^{-10}
3 (0+jx)	$j5\times10^{-10}$	$j5\times10^{-10}$	1×10^{-8}	0

The results for a purely resistive fault impedance, obtained from the computer program, are given in Table 3, where the fault impedances are in Table 3(a).

4.2 Fault Admittance Matrix and Sequence Impedances at the Faulted Bus Bar.

The symmetrical component fault admittance matrix obtained from the program for the line-to-ground fault in Table 3(b) is equal to the theoretical value, obtained using equation (3). The self sequence impedances at the faulted bus bar obtained from the program, Table 3(c) are equal to the theoretical values.

4.3 Fault Currents

The symmetrical component fault currents obtained from the program using equations (4) and (4a) are in agreement with the theoretical values; see Table 3(d). In particular, the sequence currents for the line-to-ground fault are equal to each other and are the inverse of the sum of the sequence impedances at the faulted bus bar. This is consistent with the classical approach that connects the sequence networks in series.

The phase currents in the fault obtained from the program, Table 3(e), are in agreement with the theoretical values. In particular, the currents in the healthy phases are zero and the current in the faulted phase lags the voltage by *90°*, since the resistances in the networks are zero. It is seen that the currents in the transmission line, Table 3(i), are equal to the fault currents. Also the sum of the phase currents in the transmission line is equal to the current in the ground path.

Figure 6 summarises the transformer phase currents. The currents in the transformer, Table 3(j), on the line side, are equal to the currents in the line. Note that the fault currents only flow in the winding of the faulted phase on the earthed-star connected side. The currents at the sending end of the transformer, the delta-connected side, flow into the phase ***a*** and phase ***c*** terminals of the transformer. The current entering the phase ***b*** terminal is zero. This means that the phase fault currents only flows in the winding between terminals ***a*** and ***c***. This is consistent with the ampere turns balance requirements of the transformer. The other two windings on the delta-connected side do not carry currents as the corresponding windings on the earthed-star connected side have no current.

The phase fault currents flowing from the generator are equal to the phase currents into the transformer, Table 3(k). Phase fault currents only flow in phases ***a*** and ***c*** of the generator. It is a feature of the delta earthed-star connection that a single phase load on the star side is supplied from two phases on the delta side.

4.4 Fault Voltages

The symmetrical component voltages at the fault point obtained from the program using equation (5) are in Table 3(f). They are in agreement with the theoretical values. In particular, the sequence voltages for the line-to-ground fault summate to zero, consistent with the concept of the networks being connected in series. The phase voltages at the fault are in Table (g). Note that the phase voltage of the faulted phase is zero while the voltages in the healthy phases are of equal magnitude, and greater than unity, the rated value.

The phase voltages at the bus bars are in Table 3(h). At bus bar 2 the voltage in the faulted phase is *67%* of the prefault value while the voltages in the healthy phases are *96%* of the prefault value. At bus bar *3*, the voltages lead the voltages at bus bar *2*. In particular the voltage in the phase ***a*** leads the corresponding phase ***a*** voltage at bus bar *2* by *34.7°*. The increase in the phase shift between phase voltages of phase ***a*** is due to the voltage drop in the transformer. The voltage of phase ***b*** is equal to the pre-fault value. The phase ***b*** voltage at bus bar 3 leads that of phase ***b*** at bus bar *2* by *30°*. This is as expected since there is no current in phase ***b*** of the generator. The phase ***c*** voltage at bus bar *3* leads that of phase ***c*** at bus bar *2* by *29.6°*.

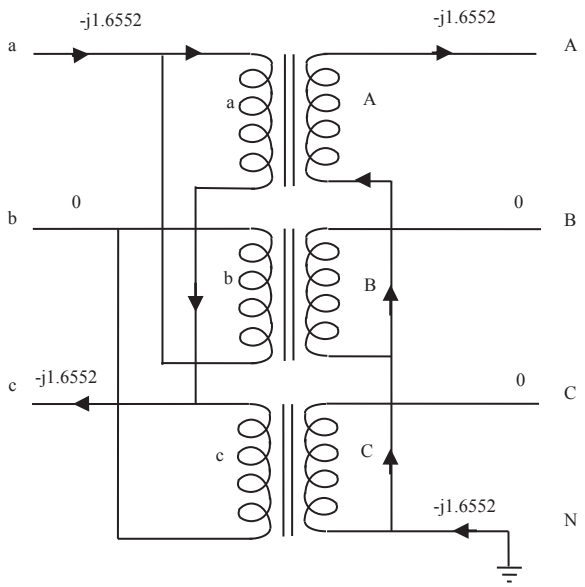

Figure 6: Transformer Currents for a Line-to-Ground Fault

4.5 Major Contribution

The major contribution of this work is the systematic iterative procedure for simulating short circuits in the general fault admittance method. The resulting fault impedances give fault current solutions that are to a specified tolerance, such as 10^{-8} per unit. Note that once the values of fault impedances to simulate short circuit faults on a particular system have been determined they need not be calculated every time the faults are solved on the same system.

4.6 Future Work

The current work has come up with a procedure for simulating zero fault impedances in the faulted phase and ground path for a line-to-ground fault. The procedure starts with low values, which are successively reduced until the solution converges to a specified tolerance, such as 10^{-8} per unit. It has been established that when the tolerance is too low the solution diverges, i.e. the tolerance is not met.

It is intended, in future work, to apply the method to practical systems, in addition to further investigating the convergence characteristics of the solution procedure. Some of the issues to be studied are the reduction factor, arithmetic precision and effect of resistance in lines.

The work used a reduction factor of 10, i.e. the fault impedance was multiplied by 0.1 to obtain the next iterative value. It would be interesting to see the effect of using other reduction factors, such as 2, 5, 15 and 20. The aspect of arithmetic precision, whether using double precision arithmetic improves the convergence, is important. This is because the effect of the unity matrix in the factor $(U+Z_{sjj}Y_{fs})^{-1}$ in equation (6) will probably

continue for lower values of fault impedances, i.e. higher values of fault admittances.

The effect of resistance in lines should be studied to establish whether the convergence characteristics are affected when the lines have resistances in them, which will be present in the self-term Z_{sjj}. This aspect should be studied when the method is applied to practical power systems, as part of the future work.

5. CONCLUSIONS

A procedure for simulating the fault impedance of a metallic line-to-ground fault has been proposed and tested. The results show that a purely resistive fault impedance gives the best convergence. For the system studied, a value of 10^{-9} per unit is found suitable. The method allows the estimated fault impedance to be reduced until the positive sequence fault current converges to a pre-set tolerance. In cases where convergence is not as good as for purely resistive fault impedances the tolerance is reduced and the convergence for the lower tolerance studied.

The line-to-ground fault is interesting for studying the delta earthed-star transformer arrangement. It is seen that although only one phase carries the fault current on the earthed-star side the currents on the delta-connected side are in two phases. Phase shifts in the transformer may be deduced from the results. The results give an insight in the effect that a delta earthed-star transformer has on a power system during line-to-ground faults.

The general fault admittance method solution of a line-to-ground fault has confirmed the main advantage of the method which is that the user need not know, beforehand, the relationships of the sequence fault currents and voltages. The user can deduce the various relationships from the results.

REFERENCES

[1] J.D. Sakala and J.S.J. Daka: "General Fault Admittance Method Solution for a Line-to-Line-to-Line-to-Ground Unsymmetrical Fault", *British Journal of Applied Science and Technology*, Vol. 4, No. 22, pp 3120-3133, June 2014.

[2] J.D. Sakala and J.S.J. Daka: "General Fault Admittance Method Line-to-Line Faults in Reference and odd phases", *International Journal of Electrical Electronics and Telecommunications Engineering*, Vol. 45, No.1, pp 1374-1383, February 2014.

[3] J.D. Sakala and J.S.J. Daka: "General Fault Admittance Method Line-to-Line-to-Ground Fault in Reference and Odd Phases", *International Journal of Engineering Research and Applications*, Vol. 4, No 2, pp.679-690, February 2014.

[4] J.D. Sakala and J.S.J. Daka: "General Fault Admittance Method Solution of a Balanced Line-to-Line-to-Line Fault", *Australian Journal of Basic and Applied Sciences*, Vol. 8, No. 1, pp 238-247, January 2014.

[5] J.D. Sakala and J.S.J. Daka: "General Fault Admittance Method Solution of a Line-to-Line Fault", *International Journal of Advanced Computer Research*, Vol. 3, No. 4, Issue 13, pp 130-138, December 2013.

[6] J.D. Sakala and J.S.J. Daka: "General Fault Admittance Method Solution of a Line-to-Line-to-Ground Fault", *Australian Journal of Basic and Applies Sciences*, Vol. 7, No. 10, pp 75-85, 2013.

[7] J.D. Sakala and J.S.J. Daka: "General Fault Admittance Method Line-to-Ground Faults in Reference and Odd Phases", *International Journal of Applied Science and Technology*, Vol. 2, No.9, pp 90-104, November 2012.

[8] J.D. Sakala and J.S.J. Daka: "Unbalanced Fault Analysis by the General Fault Admittance Method", *Proceedings of the 10th Botswana Institution of Engineers International Biennial Conference*, Gaborone, Botswana, 17-19 October 2007.

[9] O.I. Elgerd: *Electric Energy Systems Theory, an Introduction*, pp 430-476, McGraw Hill Inc., 1971.

[10] H. Sadat: *Power System Analysis*, second edition, McGraw Hill, International Edition, pp 353-459, 2004.

[11] L.L. Grisby: *Power System Analysis and Simulation*, Chapter 8, Boca Raton CRS Press LLC, 2001.

[12] J.C. Das: *Power System Analysis*, Short circuit load flow and harmonics, Marcel Dekker Inc., pp 1-71, 2002.

[13] M. El-Hawary: *Electrical Power Systems Design and Analysis*, IEEE Press Power Systems Engineering Series, pp 469-540, 1995.

[14] P.M. Anderson: *Analysis of Faulted Power Systems*, IEEE Press, 1995.

Table 3: Simulation Results - Unbalanced Fault Study

General Fault Admittance Method – Delta-star Transformer Model

a) Fault Impedances

$$\begin{bmatrix} Z_{af} \\ Z_{gf} \end{bmatrix} = \begin{bmatrix} 5\times10^{-10} \\ 5\times10^{-10} \end{bmatrix} \qquad Z_{bf} = Z_{cf} = \infty$$

b) Symmetrical Component Fault Admittance Matrix

$$Y_{fs} = 3.3333\times10^{8}\begin{bmatrix} 1 & 1 & 1 \\ 1 & 1 & 1 \\ 1 & 1 & 1 \end{bmatrix}$$

c) Thevenin's Symmetrical Component Matrix at Faulted Bus Bar

$$Z_{sjj} = j\begin{bmatrix} 0.5 & 0 & 0 \\ 0 & 0.5 & 0 \\ 0 & 0 & 0.8125 \end{bmatrix}$$

d) Symmetrical Component Fault Currents

Current Component	Simplified Method	General Method
	Magnitude/Angle	Magnitude/Angle
+ve	0.5517 ∠ -90°	0.5517∠ -90°
-ve	0.5517 ∠ -90°	0.5517∠ -90°
0	0.5517 ∠ -90°	0.5517∠ -90°

e) Fault Current in Phase Components

Phase Component	Magnitude/Angle
a	1.6552 ∠ -90°
b	0 ∠ 0°
c	0 ∠ 0°
Ground	1.6552 ∠ -90°

f) Symmetrical Component Voltages at Faulted Bus Bar

Voltage Component	Magnitude/Angle
+ve	0.7241 ∠ 0.0000°
-ve	0.2759 ∠ 180°
0	0.4483 ∠ 180°

g) Phase Voltages at Faulted Bus Bar

Phase Component	Magnitude/Angle
a	0.0000 ∠ 133.8161°
b	1.0964 ∠ 232.1729°
c	1.0964 ∠ 127.8271°

h) Postfault Voltages at Bus Bars

Bus Bar Number	Phase a	Phase b	Phase c
	Magnitude/Angle	Magnitude/Angle	Magnitude/Angle
1	0.0000 ∠ 133.8161°	1.0964 ∠ 232.1729°	1.0964 ∠ 127.8271°
2	0.6690 ∠ 0.0000°	0.9613 ∠ 244.2278°	0.9613 ∠ 115.7242°
3	0.8788 ∠ 34.6780°	1.0000 ∠ 270.0000°	0.8788 ∠ 145.3220°

i) Postfault Currents in Lines

Line no.	SE Bus	RE Bus	Phase a Magnitude/Angle	Phase b Magnitude/Angle	Phase c Magnitude/Angle
1	2	1	1.6552 / -90.0000°	0.0000 / -26.5661°	0.0000 / 206.5651°
1	1	2	1.6552 / 90.0000°	0.0000 / 153.4349°	0.0000 / 26.5651°

j) Postfault Currents in Transformers

Trans no.	SE Bus	RE Bus	Phase a Magnitude/Angle	Phase b Magnitude/Angle	Phase c Magnitude/Angle
1	3	2	1.6552 / 270.0000°	0.0000 / -78.6901°	1.6552 / 90.0000°
1	2	3	1.6552 / 90.0000°	0.0000 / 270.0000°	0.0000 / 270.0000 °

k) Postfault Currents in Generators

Gen no.	SE Bus	RE Bus	Phase a Magnitude/Angle	Phase b Magnitude/Angle	Phase c Magnitude/Angle
1	4	3	1.6552 / 270.0000°	0.0000 / 90.0000°	1.6552 / 90.0000°

A NEW FRAMEWORK FOR DAY-AHEAD ELECTRICITY MARKET BASED ON INFORMATION TRANSPARENCY BEFORE MARKET SETTLEMENT

H. Moazzen* and M.T. Ameli*

** Faculty of Electrical and Computer Engineering, Abbaspour College of Technology, Shahid Beheshti University, Tehran, Iran.*
E-mail: hamze.moazzen@gmail.com , m_ameli@sbu.ac.ir

Abstract: This paper studies the impact of information transparency on power market; the importance and the advantages of the information transparency in power markets are described. Market price before market settlement is considered as released information and a new mechanism for observable day-ahead market is proposed. In this mechanism, participants' bidding and the market clearing model are performed in an iterative procedure which consists of a number of market rounds. The round with the most social welfare is proposed as the market settlement round. GENCOs bid using market price forecasting method. To take into account the released information, a decision-making method is presented. A six-bus test system is employed to illustrate the proposed method. The numerical results show the impact of information transparency on the market indexes. As a result, it is found that higher information transparency leads to a decreased market price and it can improve market efficiency and stability.

Keywords: Power electricity market, day-ahead market, information transparency, observable market, market settlement.

1. INTRODUCTION

In buying and selling electric energy, there are a great number of power systems in which restructuring the system has led to formation of competitive markets. In most of the power markets worldwide, a significant amount of the electric power is allocated through day-ahead markets. The importance of a day-ahead market is due to its price incentives for other markets and its arousing interest upon investing in power industry [1, 2]. Although there are several clearing mechanisms for day-ahead markets, the objective function in each case is to maximize the social welfare. The social welfare, i.e. global surplus, is defined as the sum of producer's and consumer's surplus [1, 2].

In each market, after collecting participants' bids, the Independent System Operator (ISO) clears the market, then, it publishes the results [1, 2]. As a highly common issue in power markets worldwide, during market settlement procedure, participants neither are allowed to revise their bids nor have the permission to observe their rival bids. In other words, in current power markets, participants' bids are non-observable and their offering the bids takes place solely in one step.

In most of the power markets, for instance, PJM and Australian Energy Market Operator (AEMO), even after the market is cleared, parts of information __including bidding data__ are kept secret [3-5]. While, on the contrary, microeconomic theory emphasizes the impact of information transparency on market efficiency and liquidity [6]. Plus, information transparency not only encourages the agencies to invest in power industry, but also makes the market more trustable for participants [7].

This paper presents a modelling, based on information transparency, for day-ahead power markets. In order to study information transparency in a power market, a part of information should be supposed as released information. The supposed part in this paper is market price before market settlement. This paper also proposes a new mechanism for observable day-ahead markets and describes a method for determining the result of market settlement. The method of bidding decision-making for the generation companies (GENCOs) and the market clearing model are described, too. Finally, a test case and the simulation's results are presented to illustrate the proposed method.

The remainder of this paper is organized as follows: in Section 2, information transparency in power markets is studied. Section 3, presents a mechanism for observable day-ahead market, and in Section 4, the results of a case study are analysed in details. Finally, Section 5 draws several dominant conclusions.

2. INFORMATION TRANSPARENCY IN POWER MARKETS

2.1 The Importance of Information Transparency

The microeconomic theory introduces the perfect competition market as the most competitive type of markets. In perfect competition market, all market participants are price-takers, thus, market participants cannot affect market price. In this situation, market price is equal to marginal cost of production [6, 8].

Providing sufficient Information is one of the features of a perfect competition market: market participants should be aware of the market price, the rival's bidding prices, and the characteristics of production technologies [6, 8]. The closer market gets to perfection, the more efficient it becomes. An increased market efficiency raises the social

welfare in short-run horizon, and in long-run horizon, it leads to an optimal allocation of market resources [1, 2]. Information transparency in power markets can bring advantages some of which are listed below:

- reduction in participants' financial risk
- elimination of information asymmetry
- market liquidity growth
- simplicity in market monitoring
- investment encouragement

2.2 Information Transparency Status in current Power Markets

In [9, 10], information deficit is introduced as a drawback to power markets efficiency. Reference [11] shows that immediate price reports create a stable competition in power markets. Reference [3] finds that higher information transparency helps market participants to make reliable decisions. Reference [12] shows that imperfect information can lower the GENCO's profit. In [7], publishing participants' characteristics yield advantages such as 1) market competition and liquidity growth, 2) financial risk reduction, and 3) market stability improvement.

According to [4, 5, 13-15], information transparency status in some power markets are shown in Table 1. Transmission line's information is completely published only in PJM and New England markets; GENCO's technical characteristics are always published as masked information; GENCO's economic characteristics are not published in any of the mentioned markets; and commonly with a delay, participant's bidding information is published as masked information. Therefore, we can conclude that the current power markets have a low information transparency.

3. MODELING OF OBSERVABLE DAY-AHEAD MARKET

3.1 Observable Market Mechanism

In this paper, the impact of information transparency on power markets is studied. We have used "observable market" to refer to transparent market. On the contrary, current power markets are called "sealed market" (SM). Considering Table 1, there are many possible ways to release power market information. Since it is the main index of market, market price is the most significant part of information in a power market. Market price is obtained collectively through information gained from market clearing procedure. Therefore, in this paper, market price is considered as released information.

In order for the participants to be able to revise their bids using released information, market price should be published before market settlement. To achieve this aim, we propose an iterative procedure for market settlement, as a method in which market participants offer their bids in several rounds. After collecting the bids and clearing the market, participants revise their bids according to the published market price. In this method, we define a round as a procedure consisting of 1) offering bids, 2) clearing market, and 3) publishing market result. For the procedure to be operationally feasible, it is important to note that the number of rounds should be limited.

We need to propose a method for determining market settlement round. In the case that the settlement round be pre-determined, it is very probable that the participants postpone offering their actual bids until that settlement round. Thus, in order to incite an honest behaviour of participants, the settlement round should not be pre-determined. Instead, we propose the round which brings the highest efficiency (the round with the most social welfare) as the settlement round. The proposed mechanism for observable market is shown in Figure 1.

3.2. Market Clearing Model

We suppose that ISO uses a security-constrained unit commitment to clear market after collecting the bids. For the sake of simplicity, we have assumed that demand is constant. Thus, only GENCOs participate in the market. ISO maximizes the social welfare amount by considering some constraints. Since demand is constant, the objective function is altered to minimize consumers' payment. Unit's startup and shutdown costs are not intended to avoid non-convex costs. Market result could be found using the following optimization [16]:

Table 1: Information transparency status in some power markets

Power Market Information		**PJM**	**New England**	**AEMO**	**England & Wales**	**Iran**
Demand Estimation		✔	✔	✔	✔	✔
Transmission Lines		✔	✔	✕	✕	✕
GENCO's Technical Characteristics		masked	masked	masked	masked	masked
GENCO's Economic Characteristics		✕	✕	✕	✕	✕
Bidding Information	Type	masked	masked	masked	masked	masked
	Delay (day)	120	180	1	1	30
Market Price	Delay (day)	1	1	1	1	1

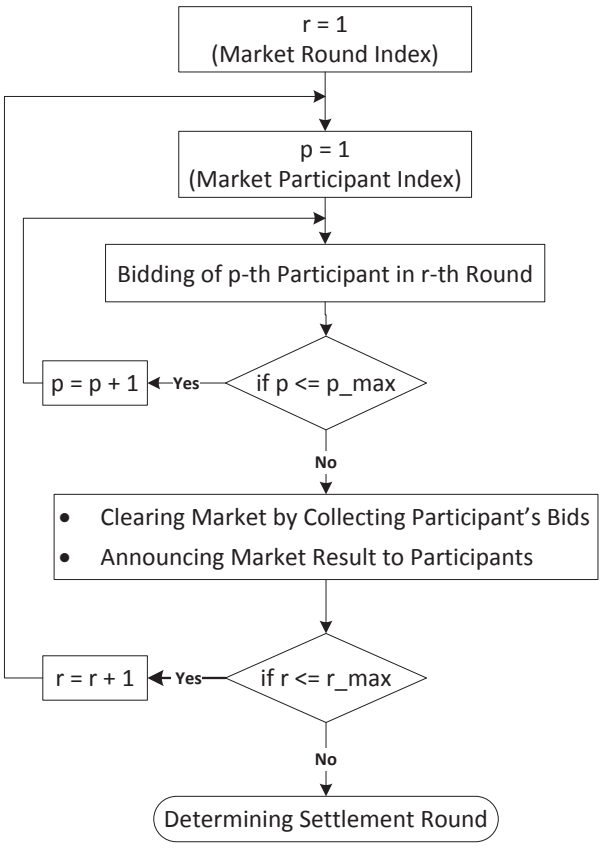

Figure 1: Observable market mechanism

$$min: \sum_{t=1}^{t_{max}} \sum_{i=1}^{i_{max}} \sum_{k=1}^{k_{max}} \{ p_k(i,t) * \pi_k(i,t) \} \quad (1)$$

Where:

t = Index of hours
t_{max} = Number of hours in planning horizon
i = Index of GENCOs
i_{max} = Number of GENCOs
k = Index of bid blocks
k_{max} = Number of allowable bid blocks
$p_k(i,t)$ = Production power of GENCO i in block k at hour t
$\pi_k(i,t)$ = Bidding price of GENCO i in block k at hour t

subject to [16, 17]:

- load equilibrium constraint
- ramp-up & ramp-down limits
- minimum uptime & downtime limits
- lines' power flow limits

3.3. GENCOs' Bidding Method

GENCOs' bidding decision-making methods are classified as below [18, 19]:

1) decision-making method based on original data
2) decision-making method based on process data
3) decision-making method based on result data.

Due to complex rules and the numerous effective parameters in power markets, only a few bidding methods can be beneficial. The first method requires rivals' technical and economic characteristics, and the second needs rivals' bidding information. As shown in Section 2, this information is not accessible in many of the power markets. In [19] and [20], this problem is introduced as the main drawback of these methods. The third method uses market price forecasting technique. This method only requires technical and economic characteristics of GENCO's own units and the public information such as historical demand and price data [21].Thus, and for a direct study on the impact of released price on participants' decisions, we employ the third method.
To reduce bidding risk, some confidence levels should be determined for forecasted price [20]. In this case, a price is figured for each confidence level, then, GENCO optimizes its production for every figured price [20]. Market price for confidence level α is provided by (2):

$$Probability(MCP_t \le MCP_{t,\alpha}) = \alpha\% \quad (2)$$

Where:

MCP_t = Market price in hour t
α = Confidence level for forecasted market price
$MCP_{t,\alpha}$ = Forecasted market price for hour t and confidence level α%.

In order to compare between observable's and sealed market's result, it is assumed that GENCOs have the same bidding method for both markets. In sealed market, GENCOs use expected value of market price which is obtained from historical market data. In the first round of observable market, GENCOs use historical data because no information is released in this round. Thus, GENCOs' bidding decisions in the first round are the same as the sealed market. In the next rounds, the price of the last round is employed by GENCOs to revise their bids. It is supposed that in the next rounds, GENCOs use a combination of the last round's price (new price) and the forecasted price based on historical data (old price). To model this combination, we suppose that each GENCO, according to its experiences and evaluations, allocates a coefficient for each price, i.e. coefficient x for old price and coefficient y for new price. For the sake of simplicity, it is assumed that $x+y=1$. Thus, $0 \le x,y \le 1$. For example, in the case that a GENCO uses only forecasted price based on historical (old price), $x=1$, and $y=0$, and when a GENCO considers these two prices with equal importance, $x=0.5$, and $y=0.5$. So to obtain the expected value of market price for the next rounds ($r>1$), we propose the following equation:

$$MCP(t)^r_{expected} = \frac{x * MCP(t)_0 + y * MCP(t)^{r-1}_{market}}{2} \quad (3)$$

Where:

$MCP(t)^{r}_{expected}$ = Expected value of market price at hour t in round r
$MCP(t)^{r-1}_{market}$ = Market clearing price at hour t in round r-1(new price)
$MCP(t)_0$ = Expected value of market price at hour t based on historical data (old price)
x = Coefficient for effect of forecasted price based on historical data (coefficient for old price)
y = Coefficient for effect of last round's price (coefficient for new price)

GENCO maximizes its profit for every confidence level to solve the bidding problem. Startup and shutdown costs are not intended to avoid non-convex costs. It is assumed that each GENCO has only one generation unit. Optimal production for every confidence level is obtained from (4) [17, 20]:

$$max: \sum_{t=1}^{t_{max}} \begin{Bmatrix} \lambda_{\alpha}(t) * p_i(t) \\ -\left[a_i * p_i^2(t) + b_i * p_i(t) + c_i \right] * v_i(t) \end{Bmatrix} \quad (4)$$

Where:

$\lambda_{\alpha}(t)$ = Market price at hour t for confidence level α
$p_i(t)$ = Production power of GENCO i at hour t
a_i = Coefficient for p^2 in cost function
b_i = Coefficient for p in cost function
c_i = Constant value in cost function
$v_i(t)$ = Binary variable, which is equal to 1, if GENCO i is committed at hour t; otherwise, 0

subject to [16, 17]:
- ramp-up & ramp-down limits
- minimum uptime & downtime limits

Using optimal amounts of price and power for each confidence level, GENCO provides price-quantity pairs. Then bidding curve is constructed by sorting pairs from the lowest price to the highest one [12].

4. CASE STUDY

In this Section, numerical results for a six-bus test system are presented to illustrate the proposed method. The characteristics of the generation units which are based on the data in [22] are given in Table 2. The modified network load is given in Table 3. And for this study, we have assumed market clearing mechanism to be uniform. To prevent price spikes, the market upper bound is supposed to be 40 $/MWh. Number of market rounds is assumed to be 10.
For the sake of simplicity, we suppose that all GENCOs have the same forecasted market price. We assume that market price has a normal distribution and the standard deviation is 10% of mean value [12, 23]. Number of the confidence levels and number of allowable bid blocks are considered to be 9 [20]. The coefficients x and y are considered as 0.5.

Table 2: Characteristic of generation units

GENCO	bus No.	a ($/MWh^2)	b ($/MWh)	c ($)	P_{max} (MW)	P_{min} (MW)
G1	1	0.0004	13.515	176.95	220	100
G2	2	0.001	32.631	129.97	100	10
G3	6	0.005	17.697	137.41	20	10

Table 3: Network load and forecasted price

hour	load (MW)	forecasted price ($/MWh)				
		case 1	case 2	case 3	case 4	case 5
1-8	180	13.7	14.1	14.5	16.1	17.4
9-16	230	20.9	23.2	24.7	27.1	29.3
17-24	300	31.6	33.3	34.2	36.0	38.4
WAP ($/MWh)		23.6	25.2	26.1	28.1	30.1

Forecasted market price has a significant influence on the market result. To be more precise, we consider it through five scenarios. These forecasted prices are chosen to cover a wide range of the forecasted price's variation. Hourly and weighted average prices (WAP) are shown in Table 3. The model has been solved using CPLEX under GAMS [24].
Observable and sealed markets' WAPs in a 24-hour horizon are shown in Table 4. The last row of Table 4 shows the converged value of WAP. WAP is converged to one value in all cases. As shown in Table 3, the difference between the most and the least value of forecasted WAP is equal to 6.5 $/MWh. In sealed market and in the 10th round of observable market, the difference is decreased to 2 and 0 $/MWh, respectively. As a result, the higher information transparency causes a less price deviation and a more price stability.
Figure 2 shows WAP variation over the observable market's rounds. Since the result has been the same over the rounds in case 3, in this case, the market is in a steady-state condition. We consider the price in case 3 to

Table 4: Market WAP for each case

round No.	case 1	case 2	case 3	case 4	case 5
1 (SM)	25.2	25.6	26.1	26.7	27.2
2	25.7	25.9	26.1	26.5	26.7
3	25.8	25.9	26.1	26.3	26.4
4	25.9	26.0	26.1	26.2	26.2
5	26.0	26.1	26.1	26.1	26.2
6	26.0	26.1	26.1	26.1	26.1
7	26.1	26.1	26.1	26.1	26.1
8	26.1	26.1	26.1	26.1	26.1
9	26.1	26.1	26.1	26.1	26.1
10	26.1	26.1	26.1	26.1	26.1

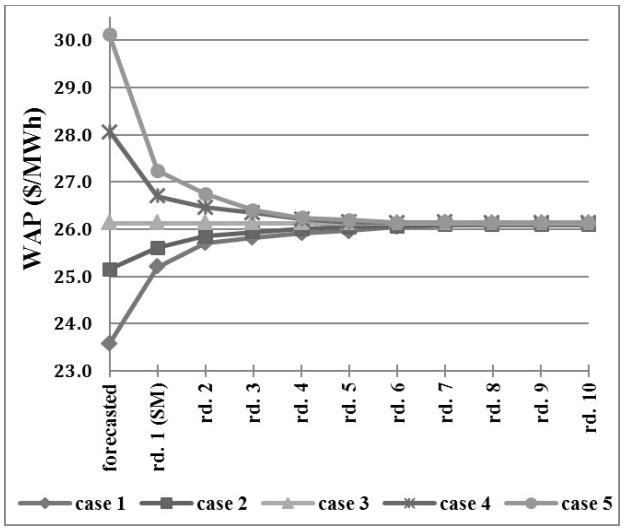

Figure 2: WAP variation over the observable market's rounds

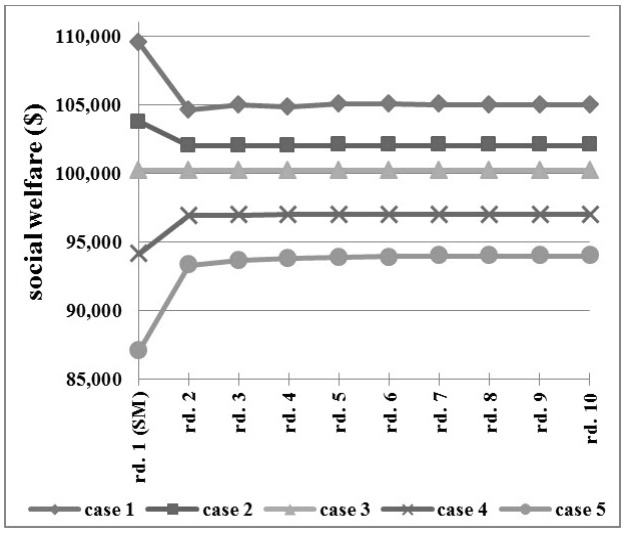

Figure 3: Social welfare variation over the observable market's rounds

be the steady-state one. In cases in which the forecasted prices are less than the steady-state price, i.e. cases 1 and 2, as the market round number increases, WAP increases up to the steady-state price. On the other hand, in cases in which the forecasted prices are more than the steady-state price, i.e. cases 4 and 5, WAP decreases down to the steady-state price. Accordingly, higher information transparency decreases the impact of price forecasting on market clearing price and therefore, this improves market predictability. Therefore, due to a higher information transparency, GENCOs' financial risk decreases.

The amount of social welfare in a 24-hour horizon is given in Table 5. As the 10th row of Table 5 shows, in all the cases, social welfare is converged, but to different values. The last row shows the market chosen (settlement) round for each case. As it can be observed from cases 1 to 5, the higher the forecasted price gets, the social welfare in the first round, i.e. sealed market, and the converged value of the social welfare, i.e. 10th round, becomes lower. As seen in Table 5, the difference between the most and the least value of social welfare in sealed market and in 10th round of observable market is equal to 22450 and 11036 $, respectively. Therefore, a higher information transparency leads to a less social welfare deviation.

Table 5: Market social welfare for each case

round No.	case 1	case 2	case 3	case 4	case 5
1 (SM)	109,523	103,778	100,211	94,139	87,073
2	104,656	102,019	100,211	96,957	93,316
3	104,966	102,030	100,211	96,992	93,676
4	104,845	102,036	100,211	97,011	93,842
5	105,067	102,039	100,211	97,026	93,920
6	105,044	102,040	100,211	97,033	93,956
7	105,032	102,041	100,211	97,038	93,972
8	105,021	102,041	100,211	97,038	93,980
9	105,021	102,042	100,211	97,038	93,985
10	105,021	102,042	100,211	97,038	93,985
chosen round	1	1	all	10	10

Social welfare variation over the observable market's rounds is shown in Figure 3. In case 3, the market is in a steady-state condition. In cases with less forecasted prices, i.e. cases 1 and 2, as market round number increases, social welfare increases and approaches the steady-state value. On the other hand, in cases with more forecasted prices, i.e. cases 4 and 5, as market round number increases, social welfare decreases and approaches the steady-state value.

Producer's and consumer's surplus and social welfare for sealed market and the 10th round of observable market are shown in Table 6 and Figure 4. In sealed market, deviation of producer's and consumer's surplus and

Table 6: Market indexes for sealed market (round 1) and observable market (round 10)

a. Producer's surplus

round No.	case 1	case 2	case 3	case 4	case 5
1 (SM)	31,382	24,908	21,390	15,257	9,488
10	26,026	23,115	21,390	18,377	14,787

b. Consumer's surplus

round No.	case 1	case 2	case 3	case 4	case 5
1 (SM)	78,140	78,870	78,821	78,882	77,585
10	78,995	78,927	78,821	78,661	79,198

c. Social welfare

round No.	case 1	case 2	case 3	case 4	case 5
1 (SM)	109,523	103,778	100,211	94,139	87,073
10	105,021	102,042	100,211	97,038	93,985

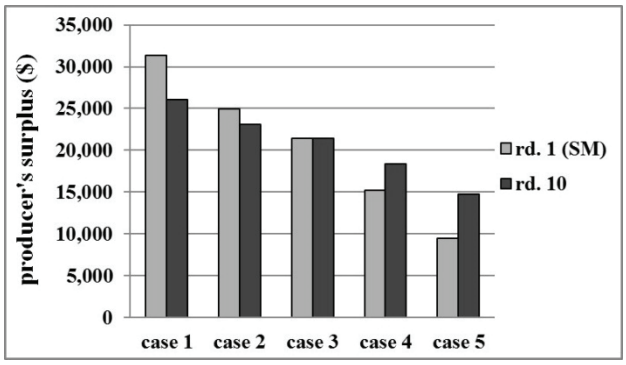

a. Producer's surplus

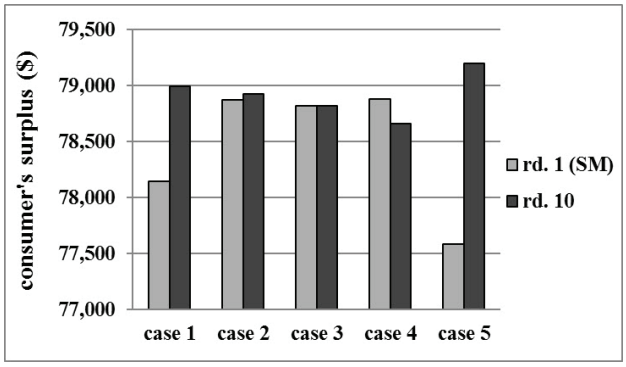

b. Consumer's surplus

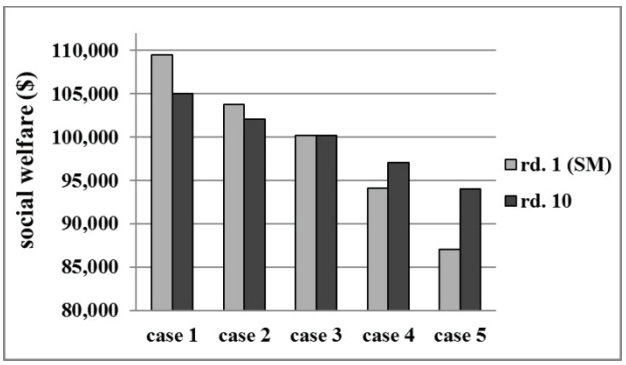

c. Social welfare

Figure 4: Market indexes for sealed market (round 1) and observable market (round 10)

social welfare is equal to 21894, 1297, and 22450 $, respectively. In the 10th observable market, these are equal to 11239, 537, and 11036 $, respectively. As a result, a higher information transparency causes a low deviation in these indexes. Thus, the impact of initial condition, i.e. price forecasting, on market indexes is reduced. This leads to an improved market stability and predictability.

The results differences in sealed market and observable market in the chosen round are given in Table 7. In cases 1 and 2, the first round is the chosen round. Thus, in these scenarios, observable market's result is exactly the same as sealed market's. In the case 3, the results of both markets are the same, as well. In cases 4 and 5, the 10th round is the chosen round. Thus, in these cases, results of sealed market and observable market are different. The results obtained from sealed and observable markets in these scenarios are compared below.

Table 7: Difference between sealed's and observable market's result in chosen round

scenarios	case1	case2	case3	case4	case5
chosen round	1	1	all	10	10
WAP	0%	0%	0%	- 2.1%	- 4.1%
producer's surplus	0%	0%	0%	20.4%	55.8%
consumer's surplus	0%	0%	0%	- 0.3%	2.1%
social welfare	0%	0%	0%	3.1%	7.9%

In cases 4 and 5, observable market's WAP is less than that of sealed market. Thus, a higher information transparency reduces market clearing price, and accordingly it decreases consumer's electricity cost. Producer's surplus is increased in both cases. Consumer's surplus is slightly decreased in case 4, but it is increased in case 5. Social welfare is raised in both cases. The increased social welfare indicates an increased market efficiency. As a result, a higher information transparency improves market efficiency in a short-run horizon.

5. CONCLUSIONS

In this paper, the impact of information transparency on power market is studied. Importance of information transparency is explained and market price before market settlement is considered as released information. A new method for observable day-ahead market is proposed. GENCOs' bidding method and market clearing model are described. A test system is employed to illustrate the proposed method. Numerical results are presented for sealed and observable markets.

The results illustrate that it is necessary to increase power market's information transparency. It is shown that the higher information transparency improves market efficiency in a short-run horizon. Also it is found that the higher information transparency reduces market clearing price and consumer's electricity cost. It is shown that the higher information transparency reduces deviation of market indexes, thus improving market stability and predictability. It is also found that the higher information transparency decreases the impact of participants' information on market result and therefore, it decreases participants' financial risk.

6. REFERENCES

[1] G. Strbac, D. Kirschen: *Fundamentals of power system economics*, John Wiley & Sons Ltd, London, UK, 2004.

[2] S. Stoft: *Power System Economics; Designing Markets for Electricity*, IEEE Press & Wiley, 2002.

[3] CRA: "Analysis of Data Release Practices in Centrally-Dispatched Electricity Markets", *International's Report to PJM Interconnection*, 2007.

[4] PJM Electricity Market's Data, Available: http://www.pjm.com

[5] Australia Electricity Market's Data, Available: http://www.aemo.com.au

[6] W. Nicholson, C. Mark Snyder: *Microeconomic Theory: Basic Principles and Extensions*, W. W. Norton & Company, 10th edition, 2009.

[7] J.D. Reitzes: "International Perspectives on Electricity Market Monitoring and Market Power Mitigation", *The Brattle Group*, 2007.

[8] H. R. Varian: *Intermediate Microeconomics*, W. W. Norton & Company, 8th edition, 2010.

[9] L. Lave, J. Apt, S. Blumsack: "Deregulation/ Restructuring, Where Should We Go From Here?", *Carnegie Mellon Electricity Industry Center*, Working Paper, CEIC-07-07, 2007.

[10] F. Wolak: "Lessons from International Experience with Electricity Market Monitoring", *University of California Energy Institute*, 2004.

[11] P.C. Carstensen: "Creating Workably Competitive Wholesale Markets in Energy: Necessary Conditions, Structure and Conduct", *Environmental & Energy Law & Policy Journal*, 2006.

[12] T. Li, M. Shahidehpour, Z. Li: "Risk-Constrained Bidding Strategy With Stochastic Unit Commitment", *IEEE TRANSACTIONS ON POWER SYSTEMS*, VOL. 22, NO. 1, 2007.

[13] New England Electricity Market's Data, Available: http://www.iso-ne.com

[14] W.H. Dunn: "Data Reqired for Market Oversight", *a concept paper for the Electric Market Reform Initiative (EMRI) of the American Public Power*, Sunset Point, LLC, 2007.

[15] Iran Electricity Market's Data, Available: http://www.igmc.ir

[16] M. Carrión, J.M. Arroyo: "Computationally Efficient Mixed-Integer Linear Formulation for the Thermal Unit Commitment Problem", *IEEE TRANSACTIONS ON POWER SYSTEMS*, VOL. 21, NO. 3, 2006.

[17] J.M. Arroyo, A. J. Conejo: "Optimal Response of a Thermal Unit to an Electricity Spot Market", *IEEE TRANSACTIONS ON POWER SYSTEMS*, VOL. 15, NO. 3, 2000.

[18] A.K. David and F. Wen: "Strategic bidding in competitive electricity markets: A Literature survey", *Proceeding Power Eng. Soc. Summer Meeting*, vol. 4, Seattle, WA, pp. 2168–2173, 2000.

[19] Z. Yang, Y. Song, R. Cao, G. Tang: "Analysis on Bidding Strategy of Power Provider by Game Theory", *proceeding on International Conference on Power System Technology*, pp. 1-6, 2006.

[20] C.P. Rodriguez, G. J. Anders: "Bidding Strategy Design for Different Types of Electric Power Market Participants", *IEEE TRANSACTIONS ON POWER SYSTEMS*, VOL. 19, NO. 2, 2004.

[21] J. Tang, J. Lin, Q. Ding, Y. Zheng: "A new optimal bidding strategy in power market", *proceeding on IEEE/PES Transmission and Distribution*, Dalian, China, pp. 1-5, 2005.

[22] Available: http://motor.ece.iit.edu/Data/PCUC_6bus.doc

[23] M. Shahidehpour, H. Yamin, and Z. Li: *Market Operations in Electric Power Systems*, New York, John Wiley, 2002.

[24] GAMS Release 23.7.3, A User's Guide, Tutorial by Richard E. Rosenthal, *GAMS Development Corporation*, 2010, Avaiable: http://www.gams.com.

EFFECT OF TEMPERATURE VARIATIONS ON WAVE PROPAGATION CHARACTERISTICS IN POWER CABLES

C. Nyamupangedengu, M. Sotsaka, G. Mlangeni, L. Ndlovu and S. Munilal

School of Electrical and Information Engineering, University of the Witwatersrand, Johannesburg, P. Bag, 3, Wits 2050, South Africa, E-mails: cuthbert.nyamupangedengu@wits.ac.za; msotsaka@gmail.com;mlangenigd@gmail.com;ndlovuls@eskom.co.za; Suneshnee.Munilal@sibanyegold.co.za

Abstract: Partial discharge (PD) mapping and fault location in power cables are techniques based on the principle of time domain reflectometry (TDR), a phenomenon that in turn depends on the high frequency wave propagation characteristics of the power cable. Furthermore, power cables are increasingly being used to simultaneously convey electric energy as well as communication signals in technologies such as smart grids. In operation, power cables experience wide ranging temperature variations due to changes in the load current flowing through the cable. It is therefore necessary to understand the effect of temperature variations on the high frequency characteristics of power cables. Simulations and experimental tests performed in this study show that temperature variations introduce errors in TDR measurements. It is also shown that when temperature in the cable changes from 22°C to 58°C, attenuation increases by one order of magnitude while the propagation velocity increases by an average of 4 %. The phase constant however decreases by an average of one order of magnitude. The implications of the findings are that temperature effects have to be taken into account when designing communication channels in power cables.

Keywords: Power cables, partial discharges, TDR, smart grids, PLC, temperature, attenuation, phase constant, propagation velocity.

1. INTRODUCTION

Underground power cables are the main arteries of electric power transmission and distribution especially in environmentally sensitive areas such as cities, mining and industrial facilities. Space restrictions, safety and pollution concerns make underground power cables a favourable technology in the conveyance of electric power in densely populated areas.

In the renewable electric power industry, offshore wind farms are a common feature. Wind power stations are installed in locations that are several kilometres into the sea. The generated electricity has to be transmitted back onshore and currently the most feasible technology is the use of submarine power cables [1]. Similarly, supply of electricity to small islands near mainland is normally achieved through use of submarine power cables. Underground power cables are therefore an essential part of electric power systems.

In the power cable technology since the 60s, extruded solid dielectric cables have grown in popularity such that currently it is the first choice cable technology [2]. Other power cable technologies such as Oil Filled Cables (OFC), Gas Filled Cables (GFC) and Paper Insulated Lead Covered Cables (PILC) are nonetheless still in use especially in older installations. Most power cable circuits however now comprise of extruded insulation such as cross-linked polyethylene (XLPE).

Unlike communication cables, power cables have more complex structure as they are designed for high currents and high electric fields. Power cables are primarily designed for electric power transfer and yet are now increasingly used for simultaneous conveyance of electric power at 50 or 60 Hz together with communication signals; and this is in technologies such as smart grids, diagnostic techniques and power line communication (PLC) [3].

A peculiarity of power cables is that the cables experience wide ranging cyclic temperature variations as the electric power magnitude being drawn through the cables change in accordance with the time-dependent power demand profile. The power cable material parameters (and especially those that affect communication signals) can change significantly with variations in temperature. Temperature variations in a power cable can therefore create a dynamic behaviour of the power cable's communication abilities, a phenomenon that communication engineers need to understand in order to effectively design communication channels in power cable networks.

Time domain reflectometry (TDR) and PLC are the most common high frequency signal transfer technologies implemented in power cable systems. Each of these techniques is briefly reviewed in the following sub-sections.

1.1 Time domain reflectometry (TDR) in cable fault and PD location techniques

In electrical power cable systems, it is essential to detect and locate faults and defects and then make the necessary corrective measures. While a cable is in operation, a malfunction can occur such as an electrical short or open

circuit. When an electric fault occurs in the power cable, the attendant protection systems (such as overcurrent protection and/or earth fault protection systems) operate to switch off the affected cable from the circuit. The faulty part of the cable has to be located, accessed and repaired. In most cases the cable would be buried underground such that the problematic portion of the cable has to be accurately predicted prior to digging up for repair. Similarly incipient defects can develop during the course of operation of a power cable and this mostly occurring in vulnerable accessories such as joints and terminations. Most of these defects are associated with partial discharge (PD) activity. Such defects need to be identified, located and the necessary maintenance and/or operation decisions implemented to proactively avert unplanned power flow interruptions.

The common method in cable fault location is time domain reflectometry [4]. In such technology, an impulse voltage is injected at one end of the cable and the resultant multiple reflections are detected and analysed. Using time of flight difference or time of arrival and the propagation velocity in the cable, the location of the cable impedance change due to the fault can be determined. The same principle of TDR or the equivalent frequency domain reflectometry (FDR) are used in locating PD sources in the cable; a technique now commercially referred to as PD mapping [5-7].

Since power cables in operation experience wide ranging temperature variations due to variations in load current flowing in the cable, a question arises; do temperature variations in the power cable affect the efficacy of TDR techniques and especially under online conditions?

1.2 Power line communication (PLC) techniques

The technique of superimposing high frequency communication signals on to power frequency (50 Hz or 60 Hz) in a power cable is fairly mature [8]. In some cable circuits, instead of using separate pilot communication cables to relay the protection signals for the cable from one cable end to another, the power cable itself is used as a transmission channel for its protection signals. Furthermore, other protection signals from one substation to another can be conveyed using the power cables themselves and this technique in power systems engineering is commonly known as teleprotection.

In addition to teleprotection signals, power cables can be used as transmission channels for other communication signals such as voice, SCADA (Systems Control and Data Acquisition) signals and this technology is commonly referred to as power line carrier/communication (PLC) systems [3].

With the advent of smart grid technology, PLC systems have become more important in the management of power system assets. Although power cables have been known to be typically 'harsh' communication channels [3], there is a question that researchers are still to address; to what extent do temperature variations in a power cable influence the power cable characteristics as a communication channel?

2. EFFECT OF TEMPERATURE ON TDR-BASED FAULT LOCATION AND PD LOCATION IN A POWER CABLE

Traditionally, cable fault location and PD diagnosis have been done while the cable under test is off the network; offline. In modern practice however, it is desired that shutdowns are minimised and only reserved for absolutely unavoidable circumstances. Such constraints have given rise to techniques such as online PD diagnosis [9] and travelling wave-based fault-location techniques [10-12]. In online PD detection, partial discharge signals are decoupled from the cable and processed while the cable is in its normal energised operational state. Online PD diagnosis enables continuous monitoring of PD activity in the cable in order to make more informed decisions that are based on trending PD data.

In online cable fault location, the travelling wave generated by the fault arc is processed as the fault occurs such that the fault position along the cable is determined in real time [11,12]. Such techniques shorten significantly the cable fault intervention time.

The online cable diagnosis and fault location techniques imply that it is highly probable that separate instances of measurements on the cable occur while the cable is at a temperature different from the normal ambient temperature or the temperature at which the calibration would have been done. In trending the logged PD data, if the readings are recorded at different cable temperatures, the information conveyed (and this includes PD location) may be misleading.

It is therefore important to understand how TDR measurements respond to changes in temperature in the cable. The next section reviews the theory of TDR-based measurements followed by a section in which the experimental investigation results are presented.

2.1 The concept of TDR measurements

The principle of TDR can be illustrated using a multiple reflection chart as depicted in Figure 1.

In the case of locating a PD source, the PD defect generates a pulse that splits up into two; one travelling to the near end (the measurement point) and the other to the far end. The latter reaches the far end where it is reflected back as the cable is open circuited. The reflected pulse travels back in the cable to the near end and is recorded by the oscilloscope. Meanwhile due to impedance mismatch the pulse is further reflected back into the cable. The process continues until the pulse eventually diminishes in magnitude due to attenuation. If

the pulses are generated at a regular repetition rate, a stationary record of multiple reflection pulses appears on the oscilloscope.

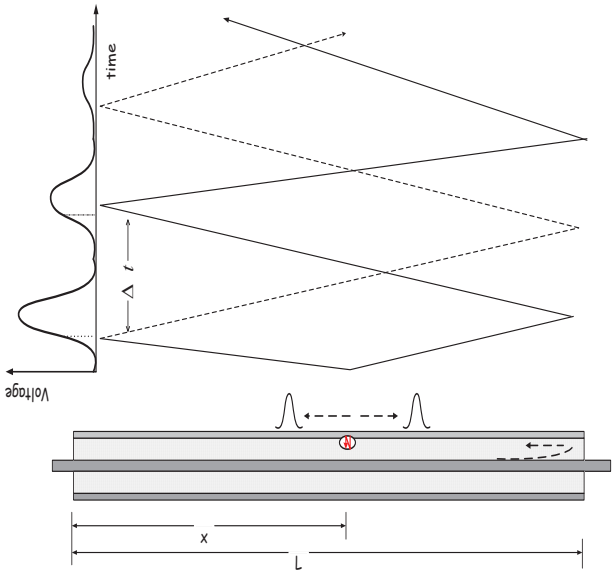

Figure 1: An illustration of how multiple reflection pulses are generated from a PD in a power cable.

If the cable length (L) is known, the location (x) of the PD source from the near end is given by equation 1.

$$x = L - \frac{1}{2}\Delta t.v \qquad (1)\ [13]$$

Where:

Δt is the time difference between the incident and the reflected pulse.
v is the velocity of propagation of the pulse in the cable.

With reference to the high frequency model of a power cable as shown in Figure 2, the insulation and semiconducting layer losses represented by (G) are known to be dependent on both frequency and temperature [14,15]. The same applies to the capacitances of the insulation and semiconducting layers represented by (C). Capacitance is a function of the material permittivity that in turn depends on frequency and temperature. Furthermore the cable's longitudinal resistance (R), being that of the metallic core and screen, changes with temperature. In essence therefore, it is anticipated that the propagation velocity depends on temperature and if that is the case, TDR measurement techniques would require that temperature variations be taken into account.

Traditionally TDR-based fault location in a cable involves a calibration procedure where the propagation velocity is determined first and then used in calculating the location in accordance with the equation 1. In such cases it is always likely that the calibration and measurements are performed while the cable is at the same temperature.

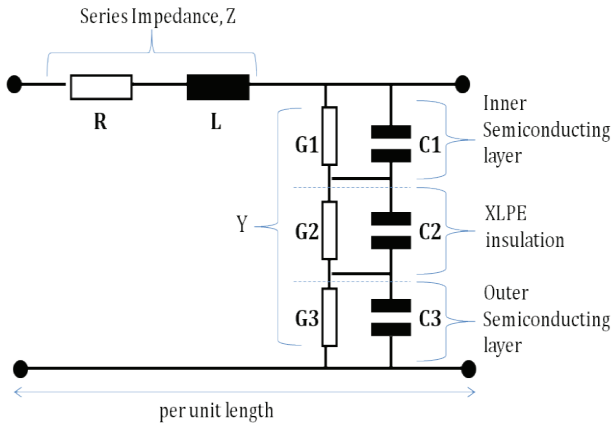

Figure 2: The power cable structure and high frequency equivalent circuit.

It can be argued that it is for this reason that in earlier literature on TDR techniques, temperature variations have not been of major interest. As an example, references [5,6], that critically review various limitations in TDR-based PD location in power cables do not mention the effect of temperature. However, with the advent of online PD mapping and innovative techniques such as fault-arc travelling wave fault location, it is highly likely that time spaced sequence of measurements on the same cable can be taken while the cable is at different temperatures. The possible influence of temperature variations on the TDR-based defect location in a power cable therefore becomes of concern in efforts on improving measurement accuracy. It is for this reason that researchers now search for further understanding of the effect of temperature on TDR techniques in power cables [14]. This paper contributes to the knowledge through a laboratory-based experimental investigation as presented in the next section.

2.2 The experimental investigation into the effect of temperature on TDR measurements

A 13 m long single core 6.3/11kV XLPE power cable was used in the experimental tests. The cable was new and its condition confirmed good through dielectric loss measurements and PD tests.

The experimental setup and procedure: The power cable was exposed to two extreme temperatures of 9°C and 75°C. The reference room temperature was taken as 25°C. The lower temperatures were achieved by cooling the cable overnight in a cold room and then performing TDR measurements as the temperature rose to room temperature. Higher temperatures were achieved though current injection. A current of 550 A was circulated in the cable core using a 0-1667 kA, 50 Hz, 3 V current injection set. The temperature would rise until the surface

temperature of the metallic sheath attained a steady state value of 75°C. The cable would then be disconnected and connected to the TDR measurement setup and measurements recorded until the temperature decreased to room temperature.

The TDR measurements were performed using the setup as shown in Figure 3. A 5 V square pulse of 5 ns rise time, 20 ns width and repetition rate of 300 kHz was injected into the cable core. The other end of the cable was kept open circuited. The resultant multiple reflection pulses were recorded at temperature intervals of 5°C. The measurements were repeated at least 3 times to ensure reproducibility.

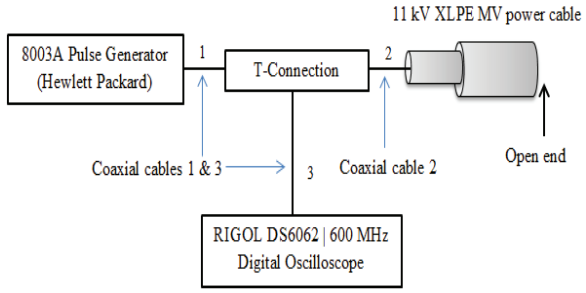

Figure 3: The TDR measurement setup.

Results analysis and discussion: The measured TDR multiple reflection pulses in the cable at different temperatures show that the pulse height, shape and relative positions change as a function of temperature as depicted in Figure 4.

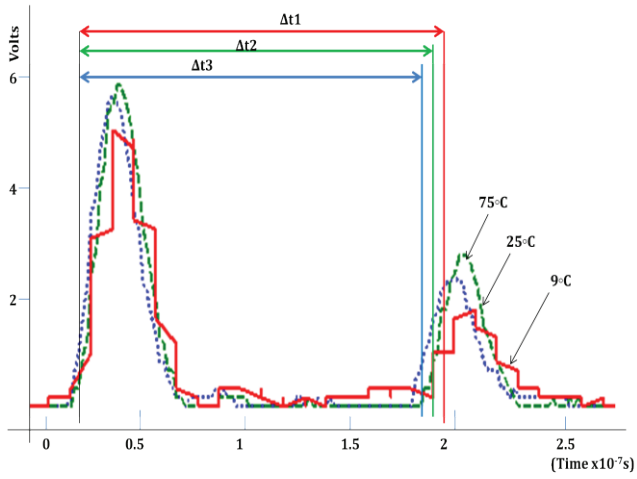

Figure 4: The measured incident pulse and first reflected pulse in a 13 m cable at different temperatures

The change of the pulse height as a function of temperature is attributed to temperature-dependent attenuation characteristics in a power cable as discussed in more detail later (Section 3) in the paper.

It is evident in Figure 4 that the inter-pulse distance reduces and the reflected pulse position shifts towards the incident pulse as the temperature in the cable increases. The time difference, Δt_1, between the incident pulse and first reflected pulse at lowest temperature (9°C), is 170 ns while that at highest temperature (75°C), is 160 ns. Assuming that changes in cable length due to temperature variations are insignificant, the corresponding propagation velocities at 9°C and 75°C are 1,63 x 10^8 m/s and 1.73 x 10^8 m/s respectively. The propagation speed increased by 6% as the cable temperature increased from 9°C to 75°C. It is concluded that the high frequency signal propagation velocity in a power cable increases with increase in temperature. These results confirm similar findings by the likes of [16] and [17].

The implications of temperature variations on the propagation velocity can be discussed in the context of accuracy in determining a PD source location using TDR. If calibration in TDR measurements (where v is determined) is done at room temperature and yet PD mapping measurements are performed online while the cable is on full load (temperature at 75°C), then the location error can result in digging out a wrong portion of the cable for repair.

It is therefore concluded that measurements that depend on propagation velocity in a power cable should not be made on the assumption that the propagation velocity is constant. Temperature effects on the propagation velocity should be taken into account in order to minimise errors.

3. EFFECT OF TEMPERATURE ON POWER CABLE HIGH FREQUENCY CHARACTERISTICS

The increasing popularity in using power cables in the double function of power transmission/distribution and communication (smart grids, PLC and teleprotection) have motivated researchers to study and understand the high frequency characteristics of power cables [18]. Significant knowledge in that regard has been developed to the effect that there are generally agreed high frequency models of power cables [8,19]. Nevertheless more work still needs to be done to fully characterise power cables as communication channels. An area that needs specific attention in that regard is the effect of temperature variations on the high frequency characteristics of power cables. Researchers such as Gavita Mugala and others [18-20] have contributed significantly to generation of knowledge on the power cable high frequency wave propagation characteristics. It is the intention of the work presented in this part of this paper to further contribute to the knowledge domain.

3.1 High frequency characteristics of power cables: a review

The high frequency equivalent circuit of a typical coaxial power cable is generally agreed to be that presented earlier in Section 2, Figure 2. The presented structure is basic. Variations occur depending on voltage levels and

other specific application requirements. As an example some cables have screen beds and/or water blocking material. The cable used in the experimental work into investigation of the influence of temperature on the wave propagation characteristics had a screen bed as shown in the structure in Figure 5 and so the corresponding modified high frequency model is as shown in Figure 6 [18].

The high frequency model of a power cable essentially comprises of series (longitudinal) impedance, and shunt admittance, (Y). The series impedance is due to the cable metallic core and metallic shield. For a cable with copper tape metallic shield, the series impedance can be expressed as given in equation 2 and 3 [18].

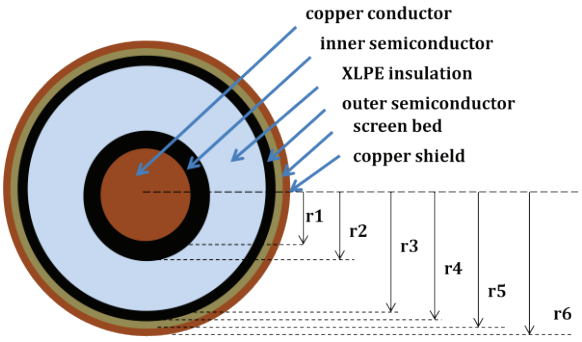

Figure 5: The the power cable with screen bed.

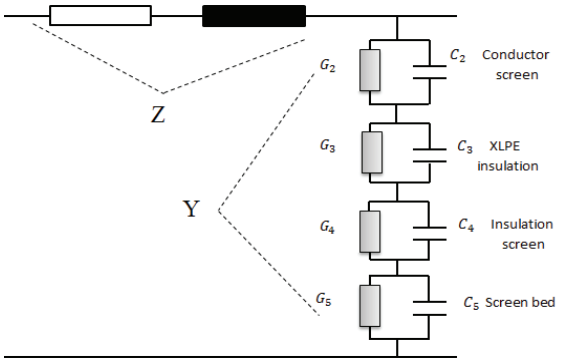

Figure 6: The high frequency model of the power cable with a screen bed layer.

$$Z = \frac{1}{2\pi r_1}\sqrt{\frac{j\omega\mu_0}{\sigma_1(T)}} + \frac{j\omega\mu_0}{2\pi} ln\left(\frac{r_5}{r_1}\right) + \frac{1}{2\pi r_5}\sqrt{\frac{j\omega\mu_0}{\sigma_6(T)}} \quad (2)\ [21]$$

$$\sigma_1(T) = \sigma_6(T) = \frac{1}{\rho(T)} = \frac{1}{\rho_{0[1+\varphi(T-T_0)]}} \quad (3)$$

Where:

r_1 and r_5 are the radii of the core and metallic sheath respectively.

$\sigma_1(T)$ is the metallic core conductivity which is a function of temperature.

$\sigma_6(T)$ is the metallic sheath conductivity which is also a function of temperature.

ω is the frequency

$\mu_0 = 4\pi$ x10^{-7} H/m is the permeability of free space

$\rho(T)$ is resistivity

φ = 3.862x10^{-3} °C is the temperature coefficient of resistivity

T_0= 20 °C

In the case of a cable with outer metallic sheath that comprises of N metallic strands each of radius, r_s, the longitudinal impedance expression is as given in equation 4 [19].

$$Z = \frac{1}{2\pi r_1}\sqrt{\frac{j\omega\mu_0}{\sigma_1(T)}} + \frac{j\omega\mu_0}{2\pi} ln\left(\frac{r_5}{r_1}\right) + \frac{1}{2\pi N r_s}\sqrt{\frac{j\omega\mu_0}{\sigma_6(T)}} \quad (4)\ [19]$$

The shunt admittance, Y, as given in equation 5 characterises the inner semiconductor, insulation, outer semiconducting layer and the screen bed. The admittance of each layer comprises of the conductance, G_k, which is essentially dielectric losses and the capacitance C_k.

$$Y = \frac{1}{\sum\frac{1}{Y_k}}, \qquad \text{where: k = 2, 3, 4, 5} \quad (5)$$

$$Y_k = G_k + j\omega C_k = j\frac{\omega\pi\varepsilon_0\varepsilon_k^*(\omega)}{ln\left(\frac{r_k}{r_{k-1}}\right)} \quad (6)\ [18]$$

Where:

ε_0 = 8.854x 10^{-12} F/m is the permittivity of free space

$\varepsilon_k^*(\omega)$ is the complex permittivity of each layer

Through measurements and curve fitting, Mugala [18] deduced an empirical expression for the complex permittivity as given in equation 7.

$$\varepsilon^*(\omega) = \frac{A_1}{1+(j\omega\tau_1)^{1-\varphi_1}} + \frac{A_2}{1+(j\omega\tau_2)^{1-\varphi_2}} + \frac{\sigma_{dc}}{j\omega\varepsilon_0} + \varepsilon_\infty \quad (7)\ [18]$$

Where:

τ_1 and τ_2 are the relaxation times.

σ_{dc} is the dc conductivity.

A_1 and A_2 are amplitude factors.

φ_1 and φ_2 are the numbers describing the broadness of the relaxation peaks.

ε_∞ is the frequency component of the relative permittivity

In high frequency techniques, communication channels are typically characterised by attenuation (α), phase constant (β), propagation constant (γ) and propagation velocity (v). With the knowledge of the parameters that influence the cable longitudinal impedance (Z) and shunt admittance (Y) then; α, β, v and Y can be analytically computed using equations 8-10.

$$\gamma(\omega) = \sqrt{ZY} = \alpha(\omega) + j\beta(\omega) \quad (8)$$

It therefore implies that:

$$\alpha(\omega) = Re(\mathrm{Y}(\omega)) \text{ and } \beta(\omega) = Im(\gamma(\omega)) \quad (9)$$

$$\upsilon(\omega) = \frac{\omega}{\beta(\omega)} \quad (10)$$

In the next section, using the geometrical dimensions and material parameters of the cable sample at hand, simulations were performed in Matlab™ to plot the variations of; α, β and v in response to temperature changes.

3.2 Simulations

The cable used in the experiment was an 8.25 long single core XLPE 6.35/11 kV 120 mm^2 copper core and copper-tape metallic sheath. The corresponding r_1 and r_5 were 6.75 mm and 23 mm respectively. The temperature-dependent parameters of the impedance (Z) and shunt admittance (Y) were deduced from the literature. Due to limitations in the availability of data on the complex permittivity of XLPE, it was assumed to be $\varepsilon_3^* = 2{,}3 - j0{,}001$ for all temperatures and frequencies [14]. The complex permittivity values of the rest of the material layers (inner and outer semiconducting layers and screen bed) were extracted from Mugala's empirical measurements at 25°C, 45°C and 65°C [18].

The simulated results of attenuation; $\alpha(\omega, T)$, phase constant, $\beta(\omega, T)$ and propagation velocity, $v(\omega, T)$ are given in Figures 7, 8 and 9 respectively.

The following distinct trends are noticeable in the simulation results:

- Signal attenuation increases with increase in frequency and temperature.
- The phase constant decreases with increase in temperature.
- The propagation velocity increases with increase in temperature.

The temperature range used in the simulations is limited to 25-65°C as this corresponded to the data available in the literature. Nevertheless the outcomes of the simulations are satisfactory as they show distinct trends that closely match practical measurements as presented in the subsequent sections.

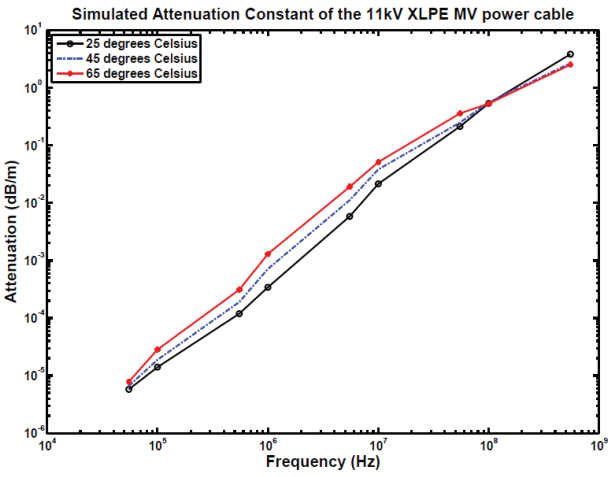

Figure 7: Simulated attenuation constant vs temperature.

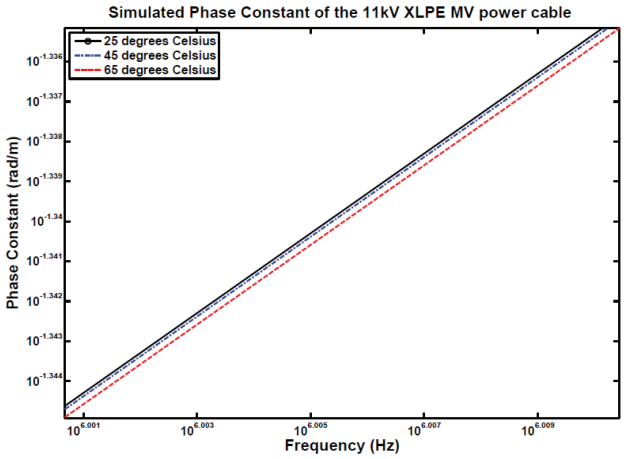

Figure 8: Simulated phase constant vs temperature.

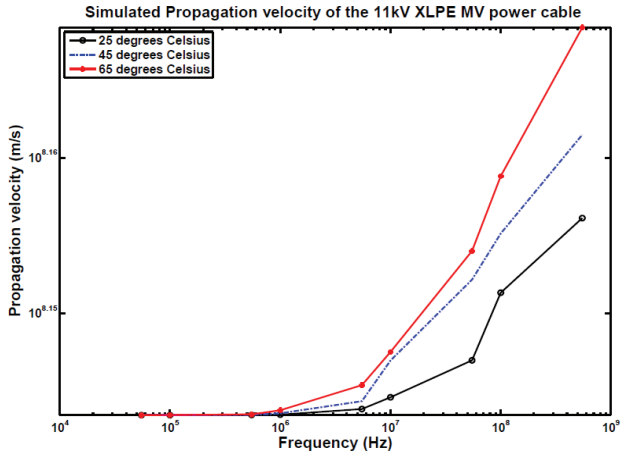

Figure 9: Simulated propagation velocity vs temperature.

3.3 The experimental tests on power cable high frequency characteristics as a function of temperature

The effect of temperature variations on the attenuation, phase constant and propagation velocity was investigated through physical measurements. Of the possible measurement techniques such as use of Network Analyser or the Standing Wave Ratio (SWR), the TDR method has been reported by other researchers to be relatively more effective in the context of the scope of this work [8,14].

A TDR measurement system similar to that presented earlier in Section 2 (Figure 3) was set up for the high frequency characterisation of the power cable.

A pulse generator was set to produce a train of square voltage pulses of 8 $V_{p\text{-}p}$, 3.7 ns rise time, 22 ns width and repetition rate of 300 kHz. Through an RG58 coaxial high frequency cable, the pulses were injected into an 8.25 m long 95 mm^2 single core XLPE 6.3/11 kV power cable. The far end of the cable was kept open circuited. Using a 1 MΩ, 600 MHz Rigol voltage probe connected to the near end of the power cable, the incident and reflected pulses were acquired and displayed in a

600 MHz, 5 Gig s/s, Rigol DS6062 Oscilloscope. An image of the multiple pulses displayed on the oscilloscope is as given in Figure 10.

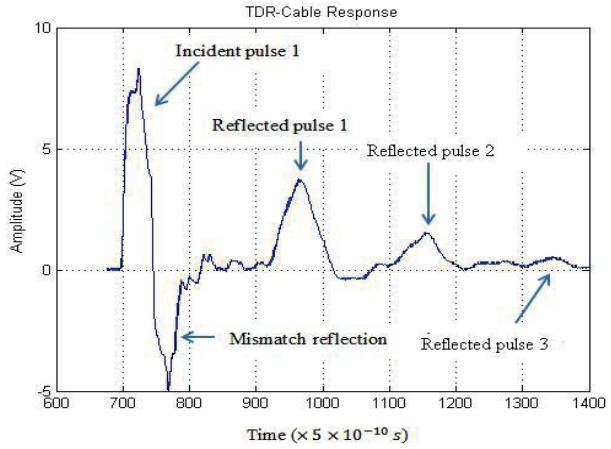

Figure 10: Measured multiple reflections.

The incident pulse 1 is launched into the power cable but due to impedance mismatch at the point of connection between the signal cable and power cable, part of the pulse is reflected back and appears as the one labelled 'mismatch reflection' in Figure 9. The rest of the energy enters the power cable and travels to the other end where it is reflected back as it encounters open circuit impedance. The reflected pulse is detected by the oscilloscope on arrival at the near end of the cable and is the one labelled 'reflected pulse 1'. Due to impedance mismatch, part of this pulse is reflected back into the cable, travels to the other end where it is reflected back yet again and detected by the oscilloscope as 'reflected pulse no. 2'.

The ratio of the Fast Fourier Transform (FFT) of the reflected pulse (V_{out}) and FFT of the incident pulse (V_{in}) gives the transfer function, $H(\omega)$, of the cable in accordance with the equation 11 [23].

$$H(\omega) = \frac{FFT(V_{out})}{FFT(V_{in})} = e^{-\gamma(\omega)2L} \qquad (11)\ [23]$$

Where:
$\gamma(\omega)$ is the propagation constant.
L is the cable length. The factor of 2 is to take into account the round trip of the reflected pulse.

Attenuation and phase constant can be calculated using L, V_{out} and V_{in} as given in equations 12 and 13.

$$\alpha(\omega) = Re\left[-\frac{1}{2L}.ln\left(\frac{FFT(V_{out})}{FFT(V_{in})}\right)\right] \qquad (12)$$

$$\beta(\omega) = Im\left[-\frac{1}{2L}.ln\left(\frac{FFT(V_{out})}{FFT(V_{in})}\right)\right] \qquad (13)$$

Equations 10, 12 and 13 for the propagation velocity, attenuation and phase constant respectively were implemented in Matlab™ processing the multiple pulse reflection data acquired using the oscilloscope in the TDR setup. Prior to the Fourier Transformation of V_{out} and V_{in}, the values are padded with zeros up to the length $n = 2^x$ for $x = 10$. The sampling rate in the Matlab™ was set at 2 GHz in order to match that of the oscilloscope.

The results of the physically measured attenuation, phase constant and propagation velocity as a function of temperature in the cable are as shown in Figures 11, 12 and 13 respectively.

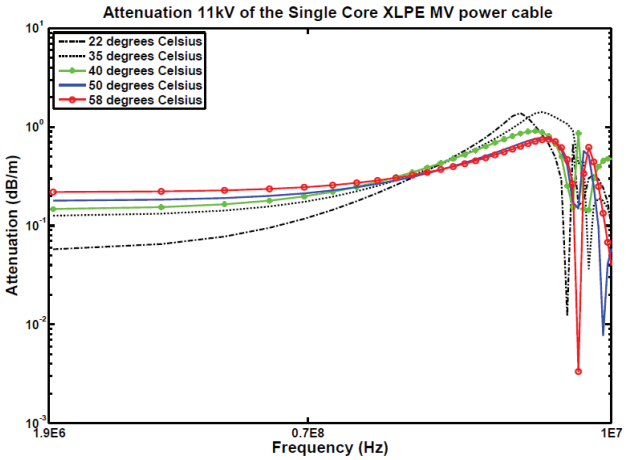

Figure 11: The measured attenuation vs temperature.

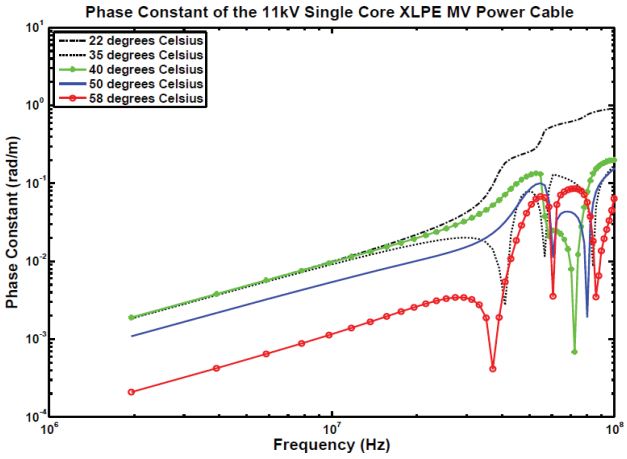

Figure 12: The measured propagation constant vs temperature.

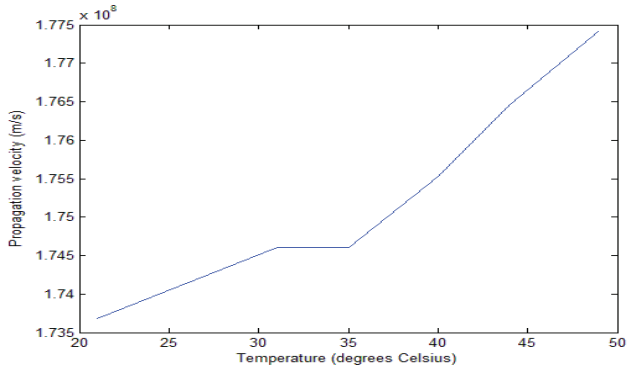

Figure 13: The measured propagation velocity as a function of temperature.

Attenuation constant dependency on temperature: At room temperature (25°C), the average attenuation of the cable value is in the order of $0.5x10^{-2}$ and it increases non-linearly with frequency. The measured attenuation values are consistent with values reported by other researchers as shown in Table 1, however notwithstanding deviations arising from variations in material composition and construction.

Table 1: Measured attenuation values in the literature

Attenuation Frequency range (dB/m)	Frequency range (MHz)	References
$0,5x10^{-2}$ - $2x10^{-1}$	10 - 10^{1}	This paper
10^{-4} - 10^{-1}	10^{-2} - 10^{1}	Tozzi et al [19]
10^{-3} - 10^{-1}	10^{0} - 0^{1}	Mugala et al [18]
0.002	10^{-1} - 10^{1}	Hashmi et al [22]

A notable characteristic of the attenuation in the power cable is that the attenuation increases by an order of magnitude when the temperature increases from 25°C to 58°C. The change is non-linear and is more pronounced at lower frequencies. As frequency approaches the bandwidth upper limit of the cable (17.5 MHz) the differences in attenuation at different temperatures diminishes.

Phase constant dependency on temperature: The phase constant increases with increase in frequency but decreases by an order of magnitude as the temperature increases from 25°C to 58°C. The temperature dependent change is non-linear such that the change is higher at higher temperatures. Beyond 17.5 MHz, the signal is noisy and marks the upper cut off frequency of the power cable high frequency response.

Propagation velocity dependency on temperature: Figure 12 shows that the propagation velocity of high frequency signals in a power cable increases with increase in temperature; an average increase of 4% as the temperature increased from 25°C to 58°C. At room temperature of 25°C the measured propagation velocity was $1.74x10^{8}$ m/s which is within the order of magnitude of about 58% that of light as reported by other researchers [23].

3.4 Mathematical versions of the measured temperature dependent cable high frequency parameters

The experimental findings presented graphically in the preceding section 3.2 show that the attenuation, phase constant and propagation velocity in XLPE power cables is a function of both frequency and temperature as presented in Figures 10-12. It is therefore imperative to factor in temperature effects when designing communication channels in shielded power cables. Ideally a designer would conveniently require analytical expressions for the attenuation, phase constant and velocity. The ongoing work by the authors aims at producing single mathematical expressions in the forms; $\alpha(f,T)$; $\beta(f,T)$ and $v(f,T)$. Meanwhile the curve fitting tools in Matlab™ have been applied on Figures 11, 12 and 13 to deduce the mathematical expressions for the measured attenuation, phase constant and velocity as given in Table 2 for temperatures; 25°C, 45°C and 60°C.

Table 2: Mathematical expressions for $v(f,T)$, $\alpha(f,T)$ and $\beta(f,T)$ of a shielded XLPE power cable

Temperature	25°C	45°C	60°C
Attenuation	$\boldsymbol{\alpha(f) = Ae^{bf}}$ Where: $A = 0.4$ $b = 4.5\text{exp}(-8)$ $f = frequency$	$\boldsymbol{\alpha(f) = Ae^{b'f}}$ Where: $A = 0.4$ $b' = 3.3\text{exp}(-8)$ $f = frequency$	$\boldsymbol{\alpha(f) = Ae^{b''f}}$ Where: $A = 0.4$ $b'' = 1.5\text{exp}(-8)$ $f = frequency$
Phase constant	$\boldsymbol{\beta(f)_{25} = mf + c}$ Where: $m = 6.6\text{exp}(-8)$ $c = 0.01$ $f = frequency$	$\boldsymbol{\beta(f)_{45} = mf + c'}$ Where: $m = 6.6\text{exp}(-8)$ $c' = 0.009$ $f = frequency$	$\boldsymbol{\beta(f)_{60} = mf + c''}$ Where: $m = 6.6\text{exp}(-8)$ $c'' = 0.003$ $f = frequency$
Propagation velocity	$\boldsymbol{v(f)_{25} = Ae^{bf} + Ce^{df}}$ Where: $A = 1.4\text{exp}(8)$ $b = 5.7\text{exp}(-11)$ $C = -7.9\text{exp}(5)$ $d = -1.1\text{exp}(-7)$ $f = frequency$	$\boldsymbol{v(f)_{45} = Ae^{b'\left(\frac{f-\partial}{\sigma}\right)} + C'e^{d'\left(\frac{f-\delta}{\sigma}\right)}}$ Where: $A = 1.4\text{exp}(8)$ $b' = 5.5\text{exp}(-3)$ $C' = -3.2\text{exp}(5)$ $d' = -5.4$ $\delta = 8.0\text{exp}(7)$ $\sigma = 1.8\text{exp}(8)$ $f = frequency$	$\boldsymbol{v(f)_{60} = Ae^{b''\left(\frac{f-\partial}{\sigma}\right)} + C''e^{d''\left(\frac{f-\delta}{\sigma}\right)}}$ Where: $A = 1.4\text{exp}(8)$ $b'' = 7.04\text{exp}(-3)$ $C'' = -1.1\text{exp}(6)$ $d'' = -3.3$ $\delta = 8.0\text{exp}(7)$ $\sigma = 1.8\text{exp}(8)$ $f = frequency$

4. DISCUSSION

Attenuation is a measure of the loss of signal strength as it travels in a communication channel. In power cables, attenuation is comparatively orders of magnitude higher than that in communication cables. As an example, measured attenuations of the same lengths (8.25 m) of a 95 mm^2 XLPE power cable and that of 50 Ω RG58 coaxial communication cable plotted on the same axis show that the attenuation in the signal cable is about 100 times lower than that in the power cable as depicted in Figure 14. The relatively higher attenuation in power cables is exacerbated by the further increase in attenuation as the temperature increases. It is therefore more challenging to design communication channels in power cable networks such that the limitations have to be taken into account in evaluating smart grid technology data communication options.

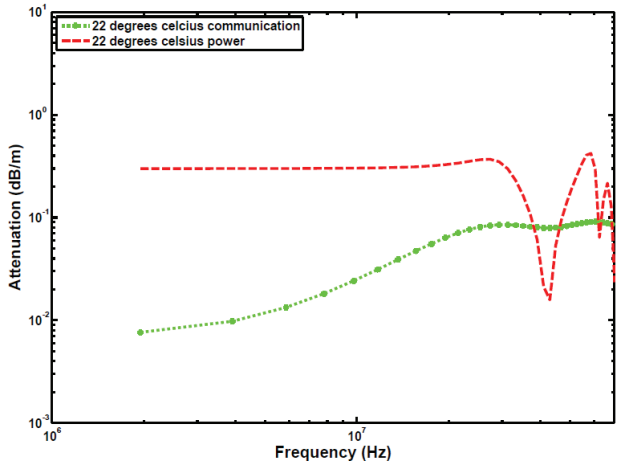

Figure 14: Attenuation profiles an 8m XLPE power cable and 8.25m 50 Ω RG58 cable.

Unlike attenuation, studies on phase constant characteristics in power cables have not been as extensive, and this is most likely because interest in power cable high frequency characteristics has mainly been motivated by PD diagnostic technology. In most PD diagnosis techniques, the phase shift of the PD signals is not as important as attenuation. However with the advent of data communication requirements in smart grids, comprehensive characterisation of the power cable as a communication medium becomes prudent. The fact that the propagation phase constant in a power cable changes significantly with variations in temperature implies that signal modulation techniques such as phase modulation that depend on the phase constant are more difficult to implement in power cables. More research efforts into further understanding phase constant characteristics in power cables are anticipated.

In the experimental measurements of the effect of temperature on power cable high frequency parameters, temperatures were measured on the surface of the metallic sheath. It is noted however that the nature of temperature distribution in power cables is such that different parts of the cable are at different temperature levels at any time. In that regard while the temperatures stated in this paper were that of the outer metallic sheath, the insulation and the metallic core would be at slightly higher temperatures. Further work in that regard therefore would be to use the measured metallic shield temperature to infer on the actual temperature of the various cable components, and this can be done using thermal models of the cable.

5. CONCLUSION

The key findings of the work presented in this paper are summarised as follows:

- The propagation velocity in power cables increases in the order of 4% as the temperature increases from room temperature to about 60°C. TDR based techniques in power cables need to take into account the temperature dependent phenomenon in order to avoid errors.
- Signal attenuation in power cables increases by an order of magnitude when the temperature is increased from room temperature (25°C) to about 60°C.
- Propagation constant in power cables decreases by an order of magnitude when the temperature in the cable increases from room temperature to about 60°C.

When designing communication channels in power cables, the influence of temperature variations on the power cable high frequency characteristics needs to be taken into account.

ACKNOWLEDGEMENT

The authors would like to acknowledge with gratitude Eskom for their support of the High Voltage Engineering Research Group through TESP. They would also like to express gratitude to the Department of Trade and Industry (DTI) for THRIP funding and to thank the National Research Foundation (NRF) for direct funding of the research group.

REFERENCES

[1] D. Zhang, J. Jung and T.J. Lieboda: 'Offshore wind parks grid connection projects in German North Sea", *Proceedings of the 8th International Conference on Power Cables,* (Jicable'2011), Versailles, France, paper A6.1, pp. 236-241, June 2011.

[2] R.Bartnikas , and K.D Srivastava, "Power Cable Engineering", *Sandford Educational Press*, Waterloo, Ontario, 1986.

[3] A. Cataliotti, V. Cosentino, P. Russotto, D. Di Cara and G. Tiné: "Experimental evaluation on narrow

band power line communication in medium voltage and low voltage smart grids", *Proceedings of the 17th IEEE International Symposium on Power Line Communications and its Applications*, (SSPLC2013), Johannesburg, South Africa, pp.35-40, March 2013

[4] S. Navaneethan, J.J. Sorghan, F. McPherson and P.F. Gale: "Automatic fault location for underground low voltage distribution networks", *IEEE Transactions on Power Delivery*, Vol. 16, No. 2, pp. 346-351, 2001.

[5] F. H. Kreuger, M.G. Wezelenburg, A.G. Wiemer and W. A. Sonneveld: "Partial Discharge Part XVIII: Errors in the location of partial discharges in high voltage solid dielectric cable", *IEEE Electrical Insulation Magazine,* Vol. 9, No.6, pp.15-22, 1993.

[6] Z. Du, P.K. Willet and M.S. Mashikan: "Performance limits of PD location based on time-domain reflectometry", *IEEE Transactions on Dielectrics and Electrical Insulation*, Vol. 4. No. 2, pp. 182-188, 1997.

[7] J.P. Steiner, P.H. Reynolds and W.L. Weeks: "Estimating the location of partial discharges in cables", *IEEE Transactions on Electrical Insulation*, Vol. 27, No. 1, pp. 44-51, 1992.

[8] A. Cataliotti, A. Daidone and G. Tiné: "A medium-voltage cables model for power-line communication", *IEEE Transactions on Power Delivery*, vol. 24, No. 1, pp. 129-135, 2009.

[9] J. Veen: "On-line signal analysis of partial discharges in medium-voltage power cables". *PhD Thesis*, Technical University of Eindhoven, 2005.

[10] M. Gilany, D. Ibrahim, and El S. Eldin: "Travelling-wave-based fault-location scheme for multiend-aged underground cable system", *IEEE Transactions on Power Delivery*, Vol. 22, No. 1, pp. 82-89, 2007.

[11] C.M. Wiggins, D.E. Thomas, T.M. Salas, F.S. Nickel and H. W. Ng: "*A novel concept for URD cable fault location*", IEEE Transactions on power delivery, Vol. 9, No. 1, 1994.

[12] Z.Q. Bo, G. Weller and M. A. Redfern: "Accurate fault location technique for distribution systems using fault-generated high frequency transient voltage signals", *IEE Proc-Gener-Trans-Distribution,* Vol. 146, No.1, January 1999.

[13] H. Borsi: "Digital location of partial discharges in HV cables", *IEEE Transactions on Electrical Insulation*, Vol. 27, No.1, pp. 28-36, 1992.

[14] V. Dubickas and H. Edin: "On-line time domain reflectometry measurements of temperature variations of an XLPE power cable", *IEEE Conference on Electrical Insulation and Dielectric Phenomena*, Kansas City, MO, pp. 47-50, October 2006.

[15] G. Tinamoto, M. Okashita, F. Aida, and Y. Fujiwara, "Temperature dependence of Tan δ in polyethylene", *Proceedings of the 3rd International Conference on Properties and Applications of Dielectric Materials,* pp. 1068-1071, Tokyo, Japan, 1991.

[16] G.M. Hashmi, R. Papazyan and M. Lehtonen: "Determining wave propagation characteristics of MV XLPE power cable using Time Domain Reflectometry technique", *International Conference on Electrical and Electronics Engineering*, Bursa, pp. I-159 – I-163, November 2009.

[17] Y. Li, P.A.A.F. Wouters, P. Wagenaars, P.C.J.M. van der Wielen and E. Fred Steennis: "Temperature dependency of wave propagation velocity in MV power cable", *18th International Symposium on High Voltage Engineering*, Seoul, Korea pp. 1861-1866, August 2013.

[18] G. Mugala: "High frequency characteristics of medium voltage XLPE power cables", *Doctoral Thesis*, The Royal Institute of Technology, (KTH), Stockholm, Sweden, 2005.

[19] M. Tozzi, A. Cavallini, G.C. Montanari, G.L. Giuliattini Burbui: "PD detection in extruded power cables: An approximate propagation model", *IEEE Transactions on Dilectrics and Electrical Insulation",* Vol. 15, No. 3, pp. 832-840, 2008.

[20] G.C. Stone and S.A. Boggs: "Propagation of partial discharge pulses in shielded power cables", *IEEE Conference on Electrical and Dielectric Phenomena,* (CEIDP), pp. 275-280, 1982.

[21] N. Pavlidou, A.J. Han Vinck, J. Yazdani and B. Honary: "Power line communications: State of the art and future trends", *IEEE Communications Magazine*, Vol. 41, No. 4, pp. 34-40, April 2003.

[22] G.M. Hashmi, R. Papazyan, M. Lehtonen: "Determining wave propagation characteristics of MV XLPE power cable using time domain reflectometry technique", *Turk. J. Ele.c Eng. & Comp. Sci.*, Vol. 19, No.2, 2011.

[23] T.R. Blackburn, B.T. Phung, M. Vakilian, M.S. Naderi and H. Zhang, "Investigation of high frequency signal propagation characteristics on HV XLPE cables", *Proceedings of the 7th International Power Engineering Conference,* (IPEC2005), Singapore, 2005.

NOTES

SAIEE AFRICA RESEARCH JOURNAL – NOTES FOR AUTHORS

This journal publishes research, survey and expository contributions in the field of electrical, electronics, computer, information and communications engineering. Articles may be of a theoretical or applied nature, must be novel and must not have been published elsewhere.

Nature of Articles

Two types of articles may be submitted:

- Papers: Presentation of significant research and development and/or novel applications in electrical, electronic, computer, information or communications engineering.
- Research and Development Notes: Brief technical contributions, technical comments on published papers or on electrical engineering topics.

All contributions are reviewed with the aid of appropriate reviewers. A slightly simplified review procedure is used in the case of Research and Development Notes, to minimize publication delays. No maximum length for a paper is prescribed. However, authors should keep in mind that a significant factor in the review of the manuscript will be its length relative to its content and clarity of writing. Membership of the SAIEE is not required.

Process for initial submission of manuscript

Preferred submission is by e-mail in electronic MS Word and PDF formats. PDF format files should be 'press optimised' and include all embedded fonts, diagrams etc. All diagrams to be in black and white (not colour). For printed submissions contact the Managing Editor. Submissions should be made to:

The Managing Editor, SAIEE Africa Research Journal,
PO Box 751253, Gardenview 2047, South Africa.
E-mail: researchjournal@saiee.org.za

These submissions will be used in the review process. Receipt will be acknowledged by the Editor-in-Chief and subsequently by the assigned Specialist Editor, who will further handle the paper and all correspondence pertaining to it. Once accepted for publication, you will be notified of acceptance and of any alterations necessary. You will then be requested to prepare and submit the final script. The initial paper should be structured as follows:

- TITLE in capitals, not underlined.
- Author name(s): First name(s) or initials, surname (without academic title or preposition 'by')
- Abstract, in single spacing, not exceeding 20 lines.
- List of references (references to published literature should be cited in the text using Arabic numerals in square brackets and arranged in numerical order in the List of References).
- Author(s) affiliation and postal address(es), and email address(es).
- Footnotes, if unavoidable, should be typed in single spacing.
- Authors must refer to the website: http: //www.saiee.org.za/arj where detailed guidelines, including templates, are provided.

Format of the final manuscript

The final manuscript will be produced in a 'direct to plate' process. The assigned Specialist Editor will provide you with instructions for preparation of the final manuscript and required format, to be submitted directly to:
The Managing Editor, SAIEE Africa Research Journal, PO Box 751253, Gardenview 2047, South Africa.
E-mail: researchjournal@saiee.org.za

Page charges

A page charge of R200 per page will be charged to offset some of the expenses incurred in publishing the work. Detailed instructions will be sent to you once your manuscript has been accepted for publication.

Additional copies

An additional copy of the issue in which articles appear, will be provided free of charge to authors.
If the page charge is honoured the authors will also receive 10 free reprints without covers.

Copyright

South African Institute for Electrical Engineers (SAIEE)
PO Box 751253, Gardenview, 2047, South Africa
Tel: 27 11 487 3003 | Fax: 27 11 487 3002
E-mail: researchjournal@saiee.org.za | Website: www.saiee.org.za